Seismicity at Newdigate, Surrey, during 2018-2019:
A candidate mechanism indicating causation by nearby oil production

Rob Westaway,
James Watt School of Engineering, University of Glasgow, Glasgow G12 8QQ, UK
robert.westaway@gla.ac.uk

Abstract
During 2018-2019, oil was intermittently produced from the Late Jurassic Upper Portland Sandstone in the Weald Basin, southeast England, via the Horse Hill-1 and Brockham-X2Y wells. Concurrently, a sequence of earthquakes of magnitude ≤3.25 occurred near Newdigate, ~4 km and ~8 km from these wells. The pattern, with earthquakes concentrated during production from this reservoir, suggests a cause-and-effect connection. It is proposed that this seismicity occurred on a patch of fault transecting permeable Dinantian limestone, beneath the Jurassic succession of the Weald Basin, hydraulically connected to the Portland reservoir via this permeable fault and the permeable calcite 'beef' fabric within the Portland sandstone; oil production depressurizes this reservoir and draws groundwater from the limestone, compacting it and 'unclamping' the fault, reaching the Coulomb failure criterion and causing seismicity. In principle this model is testable, but required data, notably the history of pressure variations in the wells, are not currently in the public domain. The recognition that this instance of seismicity is arguably caused by human activity may well help inform understanding of anthropogenic seismicity in other settings. The initial response, including claims that any connection between this seismicity and oil production was implausible, before any geomechanical analysis was done, was inappropriate.

Key words:
Anthropogenic seismicity, geomechanics, calcite 'beef', Weald Basin, Jurassic, Surrey

Introduction
A 'swarm' of earthquakes with magnitudes up to ~3, starting on 1 April 2018, has affected the Newdigate area of Surrey, in the Weald Basin of southeast England (Figures 1, 2, 3). As is detailed in the online supplement, a potential connection with local oilfield activities, in the nearby Brockham-X2Y (BRX2Y) and Horse Hill-1 (HH1) wells, was immediately suspected, but dismissed by petroleum developers (e.g., BBC, 2018; Hayhurst, 2018). Concerns about the possibility that activities in these oilfields were indeed causing these earthquakes were raised through correspondence in The Times newspaper in August 2018 (Gilfillan et al., 2018). A workshop, convened by the Oil & Gas Authority (OGA), followed on 3 October 2018, the OGA being a UK government body with responsibilities that include the licensing of exploration and development of onshore oil and gas resources in England, including managing the risk of seismicity from such operations. A summary of the proceedings of this workshop was reported (OGA, 2018), including the statement that 'the workshop participants concluded that, based on the evidence presented, there was no causal link between the seismic events and oil and gas activity although one participant was less certain and felt that this could only be concluded on "the balance of probabilities" and would have liked to see more detailed data on recent oil and gas surface and subsurface activity' (OGA, 2018, p.1). It has subsequently been argued that there is indeed no such cause and effect connection (Baptie et al., 2019; Hicks et al., 2019); developers have repeatedly issued strong public statements to this effect (e.g., BBC, 2018; Horse Hill Developments Ltd., 2018a; UKOG, 2019a). However, a major issue, not noted in any of the above-mentioned works, is the clear temporal pattern of earthquake occurrence (Fig. 4), with earthquakes strongly concentrated at times when oil is being produced from the Portland reservoir via the HH1 and/or BRX2Y wells. Production will reduce the fluid pressure in the petroleum reservoir being pumped. Fluid pressure changes within faults are well known as a cause of anthropogenic seismicity (e.g., Davies et al., 2013; Hitzman et al., 2013); however, rather than a decrease, the causative change

is usually an increase in fluid pressure as, for example, for the Preese Hall earthquake sequence in 2011, caused by injection of water under pressure during 'fracking' for shale gas (e.g., Westaway, 2017).

Figure 1 here: Map based on Hicks et al. (2019)
Figure 2 here: Cross section based on Hicks et al. (2019)
Figure 3 here: UKOGL seismic profile excerpt.
Figure 4 here: Timelines

Given the geology of the Weald Basin, a conceptual model can be envisaged whereby pressure reduction the Portland reservoir might bring nearby faults to the Coulomb condition for slip, as illustrated in Fig. 5. Nonetheless, testing this model is difficult, for several reasons. The map and cross-section reported by Hicks et al. (2019) provide the most detailed documentation of the Newdigate seismicity that is available, and thus serve as a basis for further discussion. However, a first reason why model testing is difficult is that use of these outputs is problematic because of mistakes in their preparation; before they can be used their geolocation has to be improved (this task occupies much of the present online supplement). A second reason is uncertainty in the hydraulic properties of elements of the proposed model; this includes the distribution of the permeable fabric known as 'calcite "beef"' within clay-dominated lithologies that are otherwise impermeable. Each of these aspects will be investigated in this study. A third reason why testing the proposed model is difficult is that key operational data, such as pressure variations in oil wells and logs of wellsite activities that might affect reservoir conditions, have been found to be unavailable. Indeed, preparation of this manuscript was delayed pending an attempt to obtain such data from the OGA under UK law using a Freedom of Information (FOI) request. However, this request was unsuccessful on the basis that the OGA did not hold such data, notwithstanding the extent of public interest in this topic and the statutory duties of the OGA. In the absence of pressure data, testing the proposed model will be limited to investigating the magnitudes of pressure perturbations that can be anticipated in the model fault and the time delays for their propagation between the oil reservoirs and this fault.

Figure 5 here: Cartoon illustrating conceptual model

Geological structure and stratigraphy

The study area is in southeast England, near the boundary between the counties of Surrey and West Sussex, ~40 km WSW of central London, on the northern flank of the Weald Basin (Figs 1, 6). The outcrop geology and shallow subsurface structure of this area are documented by Dines and Edmunds (1933) and Gallois and Worssam (1993); Trueman et al. (2003), DECC (2013), and others have discussed the history of petroleum exploration. Many authors have discussed the origin and structure of the Weald Basin, or Weald sub-basin of the wider Wessex Basin (e.g., Stoneley, 1982; Chadwick et al., 1983; Chadwick, 1986; Karner et al., 1987; Lake and Karner, 1987; Butler and Pullan, 1990; Hawkes et al., 1998; Andrews, 2014; Wigley, 2015; Pullan and Butler, 2018). As these and many other works demonstrate, this basin has developed near the northern margin of the Variscan orogenic belt, Variscan reverse faults having been reactivated as normal faults during the Mesozoic. Chadwick (1986) resolved two phases of Mesozoic extension in the Weald Basin, during the Early Jurassic (Hettangian to Toarcian; extension factor, β, 1.12) and Late Jurassic and earliest Cretaceous (late Oxfordian to Valangian; β=1.10). The succession of Jurassic and Cretaceous sedimentary formations that accompanied and followed this extension is documented in many works and summarised in the British Geological Survey (BGS) stratigraphic lexicon (https://www.bgs.ac.uk/lexicon/). This basin experienced Cenozoic inversion, during which some of the Mesozoic normal faults were reactivated as reverse faults (e.g., Lake and Karner, 1987). As a result of this history, some faults have normal offsets within the syn-rift succession but show reverse slip in younger sediments, as illustrated in Fig. 2. Table 1 summarises the local stratigraphy, based on the record from the HH1 well.

Figure 6 here: Fault map from Butler and Pullan (1990)
Table 1 here: Horse Hill 1 record

The oil reservoir now recognized at Horse Hill is in the Upper Portland Sandstone, with a permeability of up to ~20 mD, sealed above by the overlying impermeable Purbeck Anhydrite (e.g., Xodus, 2018; Table 1). The base of the reservoir has been inferred as in the range 580-602 m TVDSS (Xodus, 2018), thus roughly at the mid-point of the Upper Portland Sandstone. The modelled extent of this reservoir is illustrated in detail in Fig. 6.6 of Xodus (2018). At its most conservative extent, it extends for ~2 km SSE of the HH1 wellhead, ending at a contact with a fault, downthrown to the SSE by up to ~60 m, which appears to act as a seal. To the WSW the reservoir only extends for ~600 m before it is cut out by the gentle WSW dip of the base Purbeck Anhydrite. Under these conservative assumptions the reservoir has overall dimensions of ~4 km east-west by ~3 km north-south. With a base at 602 m TVDSS, this reservoir would have the same faulted contact to the SSE, but would extend for ~2.5 km SW of the wellhead, its overall dimensions being ~6 km east-west by ~4 km north-south (Xodus, 2018). The dimensions of this reservoir are not shown in Fig. 1 as its large size would clutter other detail. This reservoir, hydraulically connected to the HH1 well, is much larger than the hydraulic 'radius of influence' depicted by Hicks et al. (2019) in Fig. 1.

The base of the Jurassic sequence lies at ~2100-2200 m depth in the study area (e.g., Butler and Pullan, 1990; Pullan and Butler, 2018; Fig. 6). This sequence is locally underlain by thin Triassic deposits overlying pre-Variscan (Palaeozoic) 'basement' at depths of >~2200 m (Busby and Smith, 2001). The uppermost 'basement' in much of this area is known from borehole records to be Dinantian (Early Carboniferous) limestone (Busby and Smith, 2001; Pullan and Butler, 2018). Thus, the HH1 well log (Table 1) indicates that the Jurassic Lias Group is underlain by ~60 m of latest Triassic Penarth Group ('Rhaetic') rocks, then ~50 m of the Triassic Mercia Mudstone, then ~10 m of dolomitic conglomerate of uncertain age, then ~70 m of Dinantian limestone, above a mudstone-dominated Upper Devonian succession. Busby and Smith (2001) estimated using gravity modelling that these Devonian rocks are typically ~1-2 km thick, their base at a typical depth of ~3.5-4 km, being underlain in the central Weald Basin by many kilometres of Lower Palaeozoic metamorphic basement. Around the northern margin of the basin and the southern margin of the adjoining London Platform the Dinantian limestone and underlying Devonian rocks are well imaged seismically at <1 s two way time (TWT), indicating depth <~1500 m (e.g., Andrews, 2014). Both these subdivisions are locally several hundred metres thick, the limestone being relatively unreflective and the Devonian succession highly reflective. Moving southward, as the overlying Mesozoic succession thickens, the Dinantian limestone gradually becomes thinner and its boundaries become more difficult to interpret seismically (e.g., Andrews, 2014). Busby and Smith (2001) noted reports of this limestone in many boreholes beneath the Weald Basin; in their view it persists southward beneath most of the basin, almost to the English Channel coastline.

More recently, Pullan and Butler (2018) have presented a new map (their Fig. 21) showing the pre-Variscan subcrop beneath much of the Weald Basin (including most of the area of Fig. 1, except its NE corner) as Devonian, the Dinantian limestone being inferred to be absent. As interpreted by these workers, this limestone dies out ~2.5 km SW of the HH1 well, indicating that it is absent in the vicinity of the Newdigate fault and the associated seismicity. However, seismic lines in this area (e.g., that in Fig. 2) do not clearly resolve whether this limestone is present or not; as Pullan and Butler (2018) showed, there is no well control for ~20 km distance SW of the HH1 well, so no direct evidence either way. Pullan and Butler (2018) noted dipmeter evidence that in the HH1 well this limestone dips northward at ~20-30°; their inference that it dies out not far away seems based on structural projection given its thickness (Table 1) and assuming continued northward dip. However, it is clear from other seismic sections (e.g., Andrews, 2014) that in other parts of the basin the Dinantian limestone is folded. At this stage it is unclear whether this lithology is present across the study area or

not. The proposed conceptual model (Fig. 5) requires a highly permeable lithology, such as this, beneath the Mesozoic sediment in this area.

The two key issues already noted will now be addressed. The distribution and properties of calcite 'beef' will first be discussed. Second, the geolocation of features, mislocated by Hicks et al. (2019), will be considered.

Calcite 'beef' and its significance

Calcite 'beef', first reported by Webster (1826), consists of bedding-parallel veins of diagenetic calcite (e.g., Cobbold and Rodrigues, 2007; Zanella et al., 2015). Buckland and De la Beche (1835) adopted this nomenclature for veins of fibrous calcite within claystone beds in what is now known as the Purbeck Group in Dorset, the term 'beef' having originally been used by quarry workers on account of similarity to the fibrous structure of meat. This fabric (illustrated by many authors, including Tarney and Schreiber, 1977, Cobbold et al., 2013, and Meng et al., 2017) is now recognized in mudstone formations worldwide (e.g., Cobbold et al., 2013). Following the above-mentioned early reporting its mode of origin was widely debated; the view has become accepted relatively recently that 'beef' develops by natural hydraulic fracturing associated with overpressure during hydrocarbon maturation and migration (e.g., Parnell et al., 2000; Lash and Engelder, 2005; Cobbold and Rodrigues, 2007; Cobbold et al., 2013; Al Duhailan et al., 2015; Zanella et al., 2015; Zhang et al., 2015; cf. Maher et al., 2017; Meng et al., 2017). This fabric is indeed sometimes designated as 'hydrocarbon-expulsion fractures' (e.g., Al Duhailan and Sonnenberg, 2014). The conditions for calcite 'beef' development include palaeo-temperature in the range 70-120 °C (Cobbold et al., 2013). In the central Weald Basin, palaeo-temperatures as high as this are expected throughout the Jurassic succession, given the estimated ≥~2 km of burial during the Cretaceous sedimentation, before the Cenozoic erosion (e.g., Andrews, 2014).

In southern England, calcite 'beef' is best known in the Early Jurassic Shales-With-Beef Member (https://www.bgs.ac.uk/lexicon/lexicon.cfm?pub=SHWB) of the Charmouth Mudstone Formation, part of the Lias Group, which crops out around Lyme Regis in Dorset (e.g., Lang, 1914; Lang et al., 1923; Hesselbo and Jenkyns, 1995; Meng et al., 2017). Calcite 'beef' is also well known in the Late Jurassic of the Weald Basin from both outcrop and borehole sections (e.g., Howett, 1964). In the Howett (1964) stratigraphy, this fabric occurs within the 'Shales with Beef and Clay-ironstone' unit, which occurs at the top of the Middle Purbeck succession and is typically ~20 m thick. This fabric (reported as 'calcite veining') is also known from older Late Jurassic deposits, for example in core recovered between 701 and 710 m depth (below ground level 80.3 m O.D.) in the Collendean Farm borehole (drilled in 1964; BGS ID TQ24SW1; at TQ 2480 4429) near the Horse Hill site (Fig. 1).

In the Collendean Farm borehole log, 'beef' was interpreted as occurring in glauconitic sandstone forming the lower part of the Portland Group. However, Gallois and Worssam (1993) placed this stratigraphic level in what they regarded as the sandy upper part of the underlying Kimmeridge Clay Formation. Nonetheless, in recent petroleum exploration reports (e.g., Xodus, 2018), as in the summary in Table 1, this glauconitic sandstone with calcite 'beef' is reinstated within the Lower Portland Sandstone. Its inclusion within the Portland Group explains why this group is portrayed as much thicker in the recent petroleum-oriented literature (e.g., ~130 m thick in Table 1) than by Gallois and Worssam (1993), who gave its thickness as only 54 m at Collendean Farm. As these latter authors noted, the Portland Group in the Weald Basin is not well correlated with the 'type' Portlandian of the Portland area of Dorset, which is in the Portland – South Wight Basin, not the Weald Basin (e.g., Hawkes et al., 1998). The 'type' Portlandian includes the Portland Limestone (now known as the Portland Stone Formation), an important building stone; the sediments of this age being not sandstone-dominated as in the Weald Basin.

The significance of all the above for the present study is as follows. It has previously been noted that the combination of processes responsible for 'beef' formation will create permeability anisotropy, permeability being far greater parallel to the fabric and bedding than in the perpendicular direction (e.g., Lash and Engelder, 2005; Bisdom et al, 2016). Various workers have estimated the permeability of such bedding-parallel fractures, the highest estimate identified during the present work, ~900 mD (~9×10^{-13} m^2), being by Carey et al. (2015) for the Ordovician Utica Shale of eastern North America. This is many orders-of-magnitude higher than the expected nanodarcy permeability of shale perpendicular to bedding, and is quite a high value for rocks in general.

Other workers (e.g., Wang, 2016; Maher et al., 2017; Meng et al., 2018) have investigated the aperture, or width, of bedding-parallel fractures (typically filled with 'beef') in shale. In a study spanning several shale provinces, Wang (2016) found fractures with width varying between 15 μm and 87 mm. Many of the wider ones could be seen to form as a result of multiple increments to opening, each adding a few tens of microns of width, prior to cementation due to growth of calcite. Permeability and fracture aperture can be interrelated by comparing the Darcy equation for laminar fluid flow, $Q = (k\ A\ /\ \eta)\ dP/dx$, and the Poiseulle equation for laminar flow between parallel boundaries, $Q = (D\ W^2\ /\ (12\ \eta))\ dP/dx$, which is a solution to the more general Navier-Stokes equation for fluid flow (e.g., Zimmerman and Bodvarsson, 1996). Here Q is the volume flow rate, η the viscosity of the fluid, dP/dx the pressure gradient in the direction of flow, k the permeability of the medium, A the cross-sectional area of the flow, and W and D the width of the channel and its length in the direction perpendicular to the flow. Combining these two formulae, equating A to D×W, gives $k \equiv W^2/12$. This formula gives the permeability equivalent to W=15 μm as ~20 D (~2×10^{-11} m^2). Overall, it is inferred that the ~900 mD value, from Carey et al. (2015), rounded to ~1 D (~10^{-12} m^2), might be applicable to 'beef' in the present study area. As will become clear below, the present analysis also requires knowledge of the specific storage S_S of calcite 'beef', although no published estimate for this parameter is known to the present author. Other fractured rocks have S_S ~10^{-6} m^{-1} or thereabouts (e.g., Younger, 1993; Jones et al., 2000; Blake et al., 2010); pending any direct determination, this value will be adopted here.

Geolocation

The study area has been illustrated using the map (Fig. 1), and seismic cross-section (Fig. 2) from Hicks et al. (2019). However, the original versions of both these figures have required significant amendment regarding accuracy issues. This map was originally geolocated using geographical co-ordinates; to make it easier to use British National Grid (BNG) co-ordinates have been added. This map also shows seismic lines and faults. The source of information for positions of seismic lines, including line TWLD-90-15 that is illustrated in Figs 2 and 3, was not reported by Hicks et al. (2019); it is evident that they are from the UK Onshore Geophysical Library (OGL; https://ukogl.org.uk/) location map, which is itself indexed to the BNG, so this information must have been first transformed to geographical co-ordinates by Hicks et al. (2019). Hicks et al. (2019) also explained that (rather than using the existing literature, including geological maps and structural analyses by BGS and petroleum developers, as might be expected) they located faults in the study area through their own interpretation of 2-D seismic reflection profiles. Furthermore, the velocity model used by Hicks et al. (2019) for earthquake location (Table 2) is significantly slower than the set of interval velocities from the HH1 well (Table 1), causing their hypocentres to be mislocated at depths that are too shallow.

Table 2 here: Hicks et al. (2019) velocity model

The seismic section in Fig. 2 clearly has higher resolution than older ones, including those which informed earlier fault maps such as that by Butler and Pullan (1990) (Fig. 6). Some of the faults depicted in Fig. 2 are, thus, recognized for the first time. However, additional faults are also evident in the uninterpreted version, provided by Hicks et al. (2019) as their supplementary Figure S13, which

lacks the overwhelming interpretation applied to Fig. 2, and in the raw seismic section provided by UKOGL (Fig. 3). Of particular significance, it is suggested, is the nature of the Newdigate Fault which, in the lower part of the Jurassic sediment and upper part of the underlying Palaeozoic basement, consists of multiple fault strands distributed across a zone with width, in the north-south direction, approaching ~2 km. Careful inspection of supplementary Figure S13 of Hicks et al. (2019) and Fig. 3 indicates broken and offset seismic reflectors which delineate these subsidiary strands of the Newdigate fault zone, some evidently near the limit of seismic resolution (cf. Bond et al., 2007), which merge upwards by ~0.5 s two way time (TWT).

Depth conversion of the seismic section in Fig. 2 and location of the earthquakes, both using the same velocity model derived from the set of interval velocities (Table 1), would adjust the earthquake hypocentres downward relative to the detail in the seismic section by an estimated ~400 m (see online supplement). The key consequence of this adjustment is to move the earthquake population from within the Jurassic sedimentary section to within the Palaeozoic 'basement'. These earthquakes presumably occurred on one of the steeply north-dipping subsidiary strands of the Newdigate fault zone, given the steeply north-dipping nodal planes, identified as the fault planes, of the focal mechanisms (Fig. 1 and Table 3), rather than on the main Newdigate Fault that dips south.

The mislocation of faults in Fig. 1 is discussed in detail in the online supplement. Its most significant aspect concerns the depiction of faulting south of the Brockham oil reservoir. Figure 1 shows two faults, the Brockham Fault and Holmwood Fault, separating this reservoir from the block farther south, which leads south to the Newdigate fault zone. Hicks et al. (2019) thus proposed that the faulting in this vicinity will act as a 'baffle' to fluid flow or pressure changes, arising in the Brockham reservoir, reaching the seismogenic zone. However, when the more accurate depiction of the faulting from the petroleum industry (e.g., Xodus, 2018), is adopted, only the Brockham Fault offsets the Portland Sandstone between the Brockham oil reservoir and the seismogenic zone. Furthermore, given the seismic velocity listed in Table 1, the ~40 ms TWT offset on the Brockham Fault in this vicinity indicates a throw of ~50 m, rather less than the thickness of the Portland Group in this area (cf. Table 1). Thus, although the seal at the southern margin of the Brockham oil reservoir is provided by the downthrow against it of the impermeable Purbeck Anhydrite, the same downthrow means that at depths of a few tens of metres greater the Lower Portland Sandstone in the footwall is juxtaposed against the Upper Portland Sandstone in the hanging-wall. Since both subdivisions of the Portland Group are highly permeable, the Brockham Fault in this vicinity is unlikely to act as a 'baffle' to fluid flow or pressure changes. Amendment of the structure in this area means that reconsideration of the role of pressure changes in well BRX2Y as a causal factor for the Newdigate seismicity is warranted.

Seismicity and its correlation with well activities

As already noted, multiple publications have already documented the 2018-2019 Newdigate 'earthquake swarm', notably those by Baptie and Luckett (2018), Verdon et al. (2019), and Hicks et al. (2019). Baptie and Luckett (2018) presented a preliminary analysis of 14 earthquakes that occurred between 1 April and 18 August 2018. Their results are significant primarily because they informed the OGA workshop. The more extensive analysis by Hicks et al. (2019) will now be appraised. These latter authors determined hypocentres and other source parameters for 168 earthquakes between 1 April 2018 and 28 June 2019, some with local magnitude $M_L < -1$, their location patterns and timeline being depicted in Figs 1, 2 and 4 and summarized in Table 3. The first nine earthquakes up to 10 July 2018 (including one of the largest, with M_L 3.02, on 5 July) were located before any local seismograph stations were operational, using only data from permanent regional stations. Hicks et al. (2019) explained that due to the limited available data these events were located by assigning each a fixed focal depth. The resulting reported depths vary between 2.33 and 3.08 km (see Table S2 of Hicks et al., 2019), it being unclear on what basis different depths were assumed for different events. The next sixteen events, until 11 July, were located conventionally but including data from local stations. For

the rest of the events, both 'double difference' relocations (after Waldhauser and Ellsworth, 2000) and conventional locations were determined, using the velocity structure in Table 2. Table 4 lists earthquakes in this area that post-date the Hicks et al. (2019) study.

Table 3 here: Summary of Newdigate seismicity
Table 4 here: Most recent Newdigate earthquakes

Focal mechanisms were determined by Hicks et al. (2019) for six events, including the largest, of M_L 3.18 and moment magnitude M_W 3.25, on 27 February 2019, as illustrated in Fig. 1 and listed in Table 3. All six events have a nodal plane striking roughly east-west and dipping steeply north. As already noted, this plane is inferred to be the fault plane, indicating predominant right-lateral slip. Available data regarding the state of stress in the Weald Basin are extremely limited; Kingdon et al. (2016) and Fellgett et al. (2017) provided syntheses of in situ stress data across much of Britain. However, these authors wrote little about the Weald Basin, Fellgett et al. (2017) noting that many hydrocarbon wells in this area have yielded stress data but these data had not yet been placed in the public domain. The stress dataset available for the Weald Basin thus remains that presented by Evans and Brereton (1990). As is detailed in the online supplement, this limited dataset indicates a NW-SE maximum principal stress and a NE-SW minimum principal stress. The Newdigate earthquake focal mechanisms (Fig. 1) are consistent with this stress field orientation, given the standard requirement for the maximum principal stress to lie within dilatational quadrants (McKenzie, 1969).

Temporal clustering
As detailed by Hicks et al. (2019), the Newdigate seismicity between April 2018 and June 2019 involved four 'clusters' of activity (Fig. 4). The first began at 11:10 on 1 April (M_L 2.66), followed by two events later on the same day, another on 9 April, and a final event on 28 April. The smallest of these events (on 9 April) had M_L 1.28. No local seismograph stations were then in operation; Hicks et al. (2019) estimated that the completeness threshold for earthquake detection was circa M_L 2, so many smaller events were undoubtedly missed.

The second 'cluster' (Fig. 4) began at 12:28 on 28 June (M_L 2.52), and included four other events above M_L 2.0 (on 29 June and 5 July, and two on 18 July) including the second largest event overall (M_L 3.02), at 10:53 on 5 July. The installation of local seismograph stations in mid June and early July lowered the completeness threshold for earthquake detection to below M_L 0 (Hicks et al., 2019), resulting in many small events being thereafter detected and enabling use of the relative location procedure that was adopted. After these initial relatively large events this 'cluster' of earthquakes began to tail off, in terms of both magnitude and frequency of occurrence. The last event with M_L>0 occurred at 03:21 on 18 August (M_L 0.30), with infrequent smaller events persisting into early 2019.

The third 'cluster' (Fig. 4) began on 14 February 2019 with a relatively large event at 07:43 (M_L 2.47), followed by two other events of $M_L \geq$ ~2, at 17:03 on 19 February (M_L 1.98) and at 03:42 on 27 February (M_L 3.18), this being the largest event of the overall sequence. After these initial relatively large events this 'cluster' of earthquakes also tailed off, although two events with M_L>0 occurred during April 2019 (on 11 and 22 April; M_L 0.73 and 0.56).

The fourth 'cluster' (Fig. 4) began with a relatively large event (M_L 2.35) at 00:19 on 4 May 2019. As for the preceding 'clusters', this seismicity thereafter began to tail off, although events with M_L ~0 persisted until the end of June 2019. Locations by BGS confirm the tailing-off trend through July and August 2019 (Table 4), with a M_L 1.1 event on 2 September, three smaller events later that month, one during October, and none more before the end of 2019 (Table 3).

Overall, this pattern of seismicity, consisting of event 'clusters', each involving activity tailing off after a peak, with the largest event increasing during successive 'clusters', bears a striking resemblance to other earthquake swarms that are inferred to be caused by fluid pressure changes in a fault (e.g., Hainzl, 2004). However, the Newdigate earthquake population is insufficient to permit statistical testing of the patterns expected for this mechanism.

Correlation of seismicity with well activities

As detailed in the online supplement, during prolonged production from Brockham well BRX2Y prior to 2016, the reservoir pressure had decreased from ~900 to ~500 psi. Angus Energy (2018a) reported that at the end of production in 2016 the reservoir pressure was ~490 psi or ~3.4 MPa. At its depth of ~622 m the expected hydrostatic pressure would be ~6.1 MPa; the reservoir was evidently under-pressured. It is to be expected that flow of groundwater towards this reservoir, during 2016-2018, would re-pressurize this reservoir. Figure 4(c) indicates how the four 'clusters' of earthquakes discussed above correlate with activities affecting the Portland reservoir in the HH1 or BRX2Y wells. Production from well BRX2Y resumed in late March 2018: from Hicks et al. (2016) ~4.0 m^3 (~25 barrels) of oil were produced on 23 March followed by ~1.1, ~0.9 and ~1.0 m^3 (~7, ~6 and ~6 barrels) on 25-27 June. Reservoir pressure during this and subsequent production has not been reported, but from standard theory (e.g., Dake, 1998; Guo et al., 2008) one expects it to have decreased. This start of production occurred nine days before the first Newdigate earthquake on 1 April 2018. Furthermore, as is detailed in Fig. 4 and in the online supplement, other brief 'pulses' of production occurred from well BRX2Y in June, respectively 20, 19, 16 and 6 days before the start of the second 'cluster' of seismicity on 27 June.

Although the activities that were planned in the HH1 well in 2018 have been disclosed (Horse Hill Developments Ltd., 2018b), most of the actual activities that took place, and any associated variations in pressure within the well, have not been, other than in the very general terms reported by Hicks et al. (2019). An attempt is made in the online supplement to piece together the sequence of events, based on fragments of information available. It is thus evident that before 4 July 2018, the Portland reservoir was reported as isolated from the surface by a removable bridge plug in this well. Claims have been made that the reservoir might have been influenced before this date by surface activities at the site and by activities in the shallow part of the well (Hayhurst, 2018); if so, this would imply that the bridge plug had failed. With the exception indicated below, no pressure data from well HH1 have been made public; as already noted, an attempt to obtain such data from the OGA as a FOI request has been unsuccessful. As detailed in the online supplement, during the flow testing of the Portland reservoir in well HH1 in July-August 2018, the developer reported production rates of 140-160 bopd, with stable bottom hole pressures ~1.4 MPa below the initial reservoir pressure of ~6.3 MPa, and that bottom hole pressures recovered rapidly during periods of shut-in, indicating good connectivity within this reservoir.

It is evident from Fig. 4 that production ceased from well BRX2Y in October 2018; production at HH1 switched from the Portland reservoir to the Kimmeridgian reservoirs around the same time. Around this time, seismicity at Newdigate tailed off significantly.

The seismicity then re-intensified as the third 'cluster', recognized by Hicks et al. (2019), starting on 14 February 2019, which followed the resumption on 11 February 2019 of production from well HH1, now at rates of up to 220 bopd, from the Portland reservoir. As is detailed in the online supplement, production from this reservoir continued until late June 2019, after which it switched back to the Kimmeridgian reservoir, then during December 2019 to the newly-completed horizontal lateral, off well Horse Hill-2 (designated HH2Z), in the Portland reservoir. Seismicity at Newdigate remained significant during this phase of production from the Portland reservoir at HH1. However, production was not continuous; Hicks et al. (2019) reported shutdowns during 9-12 April and 4-10 May, the latter

corresponding to the start of the fourth 'cluster' of seismicity as recognized by these authors. Seismicity subsequently tailed off following the end of production at HH1 from the Portland reservoir in late June 2019 and the switch to production from the Kimmeridgian reservoir in early July (Fig. 4 and Table 4). Furthermore, seismicity did not resume during the initial flow testing of well HH2Z in December 2019, even though the production rates from the Portland reservoir well were much greater, up to 1087 bpd of fluid production, than they had been from well HH1 (see the online supplement).

Overall, the correlation between phases of production from the Portland reservoir, from well HH1 or well BRX2Y or both, and 'clusters' of earthquakes has been compelling (Fig. 4). Hicks et al. (2019) did not recognize this pattern, apparently because their account did not differentiate between the Portland and Kimmeridgian reservoirs as sources of production from well HH1, as is now done (based on details in the online supplement). Moreover, there are clear patterns of cause and effect for the first and third 'clusters' of seismicity: the first began 9 days after the resumption of production from well BRX2Y in March 2018; the third began 3 days after the resumption of production from well HH1 in February 2019. Nonetheless, there are no clear patterns for the other two 'clusters' of seismicity, nor any seismicity associated with the flow testing of well HH2Z during December 2019.

Conceptual geomechanical model

The conceptual geomechanical model already summarized (Fig. 5), which can account for seismicity beneath Newdigate, caused by pressure decreases in the Portland reservoir resulting from production (or other activities) from the HH1 or BRX2Y wells, will now be described in detail. The basis of this model (Fig. 5) is as follows. The Upper Portland Sandstone reservoir adjoining these wells is assumed to make a subhorizontal hydraulic connection with the seismogenic fault strand within the Newdigate fault zone via a permeable fabric formed in calcite 'beef' in the stratigraphically adjacent Lower Portland Sandstone. The seismogenic fault is assumed highly permeable and to provide a downward hydraulic connection to the rocks beneath the Jurassic succession. These rocks are assumed to include the dolomitic conglomerate and Dinantian limestone, as in the HH1 well (Table 1), which are themselves permeable. It is further assumed that the Newdigate seismicity has occurred at locations where these permeable lithologies are in contact across this fault. Pressure reduction in the Portland reservoir will thus reduce the fluid pressure in this fault, which will cause flow from within the adjoining permeable lithologies into the fault. The associated reduction in fluid volume within these lithologies will cause them to compact. This will result in surfaces in these lithologies that were previously in contact across this fault to separate slightly, reducing the normal stress across the fault. This will 'unclamp' the fault (as in Fig. 5(b)), moving it closer to the Coulomb failure condition. The fault is itself assumed to be 'critically stressed', already near this failure condition, potentially enabling relatively small change in the state of stress to cause coseismic slip (cf. Townend and Zoback, 2000; Zoback and Zoback, 2007).

Regarding the assumptions thus made, the presence of calcite 'beef' within the Portland Group sediments and its permeability have already been discussed. The permeability of faults is a major issue in Earth science (e.g., Caine et al., 1996; Evans et al., 1997; Lunn et al., 2008; Bense et al., 2013; Haines et al., 2016). There is no information regarding the permeability of any strand of the Newdigate fault zone; however, the view that faults are generally permeable, especially when critically stressed (e.g., Barton et al., 1995) is widely accepted, as is the precautionary principle that faults are assumed permeable, in the absence of contrary evidence, when assessing the possibility of subsurface fluid migration (e.g., Westwood et al., 2017; Wilson et al., 2018). Nonetheless, counterexamples exist, such as faults made impermeable by cemented fault gouge (e.g., Agosta et al., 2007). The question of the continuity of the Dinantian limestone from the HH1 area to the vicinity of the seismogenic strand of the Newdigate fault zone has already been discussed. The uncertainty regarding the state of stress in the Weald Basin is considered in the online supplement. As will become clear below, if the differential

stress here is anything like as high as it is the Preese Hall area (after Westaway, 2017), then any fault with the orientation of that which slipped will be very close to the Coulomb failure condition.

To facilitate first-order calculations regarding the feasibility of this model, the model fault is made vertical and the permeable seismogenic layer is assumed to have thickness H, hydraulic diffusivity D, hydraulic conductivity K, permeability k, and porosity ϕ. Depressurization within the Portland reservoir adjoining one or other of the nearby wells is assumed to result in a constant reduction in groundwater pressure ΔP_O at each point on the fault within the permeable seismogenic layer. As a result, the drawdown δP in groundwater pressure within this permeable layer, at a horizontal position x from the model fault at time t after the start of the imposed pressure drawdown, is given by

$$\delta P = \Delta P_O \, \mathrm{erfc} \, (x / (2 \sqrt{(D\, t)})) \qquad (1)$$

(e.g., Costain, 2017), where erfc() denotes the complementary Gaussian error function. For z>0, the function erfc(z) decreases as z increases, reaching ~0.0047 when z=2. As Detournay and Cheng (1993) noted, this condition can be taken as indicating an effective outer limit to significant pressure perturbations, at distance x_M from the model fault. It thus follows that

$$x_M = 4 \sqrt{(D\, t)} \, . \qquad (2)$$

As time progresses, an ever-widening volume of rock, perpendicular to the model fault, will thus become depressurized, water previously stored within this volume being released into the fault.

Carbonate rocks such as these are likely to be complex, being fractured, so water storage within them will be in part by opening of fractures and in part by opening of pore space. The bulk hydraulic properties already defined, D, K, k and ϕ, characterise the rock volume without consideration of such detail. However, as is well known (e.g., Newson, 1973), Dinantian limestone typically has low matrix porosity, often ~1%, its ability to store and transmit groundwater being largely via fractures. The storage capacity of an aquifer can be quantified as its specific storage, S_S, defined as the volume of water released from a unit volume of the aquifer under a unit decline in hydraulic head. By definition, S_S is related to other hydraulic properties, thus:

$$S_S \equiv K / D \, . \qquad (3)$$

K and k are interrelated thus:

$$K \equiv k \rho_W g / \eta \qquad (4)$$

where ρ_W and η are the density and viscosity of water, and g is the acceleration due to gravity. Permeability k is a constant of proportionality in Darcy's equation, which can be written thus

$$v = \frac{k \Delta P}{\eta L} \, , \qquad (5)$$

where v is the average flow velocity and ΔP is the pressure drop for flow over distance L.

Specific storage is also related to elastic moduli thus:

$$S_S = \rho_W g / B \qquad (6)$$

where B is the effective bulk modulus of the material, defined thus:

$$B \equiv 1 / ((1 / B_R + \phi / B_W) , \quad (7)$$

where B_R and B_W are the bulk moduli of the rock and water (e.g., Jacob, 1940; De Wiest, 1966). Bulk modulus is itself defined as

$$B \equiv -V \partial P/\partial V , \quad (8)$$

V denoting volume.

The poroelastic response of the rocks surrounding the model source of pressure variations in the Portland reservoir, to the imposed pressure variation, can now be investigated. In general, poroelastic responses can be complex (e.g., Detournay and Cheng, 1993). Costain (2017) applied the one-dimensional diffusion equation for the pressure of a fluid of constant density and viscosity through a medium of constant permeability,

$$\frac{\partial P}{\partial t} = D \frac{\partial^2 P}{\partial x^2} , \quad (9)$$

where t is time and x is position. He thus obtained a solution for the one-dimensional propagation (in the x-direction) of a hydraulic pressure pulse of amplitude ΔP_P and duration Δt over distance r through rocks of hydraulic diffusivity D. He showed that at times >> Δt the pressure variation δP is given to a good approximation by

$$\delta P(r,t) = \frac{\Delta P_P D r \Delta t \exp(-r^2 /(4 D t))}{2 \sqrt{\pi} (D t)^{3/2}} . \quad (10)$$

The maximum pressure perturbation at distance r occurs after a time delay t_D given by

$$t_D = r^2 /(6 D) . \quad (11)$$

It follows that the maximum pressure perturbation at distance r and time t_D is given by δP_M where

$$\delta P_M(r,t) = \frac{3 \sqrt{6} \Delta P_P D \Delta t \exp(-3 / 2)}{\sqrt{\pi} r^2} . \quad (12)$$

The alternative empirical analysis by Hettema et al. (2002), based on 'rules of thumb' rather than derivation from first principles, predicts a value for t_D that differs only by a numerical factor but does not predict pressure perturbations.

Parameter values adopted for Dinantian limestone include B_R=50 GPa and ϕ=0.04, along with Young's modulus E_R=75 GPa and Poisson's ratio ν_R=0.25, from Bell (1981), with standard values of B_W=2.2 GPa, ρ_W=1000 kg m^{-3}, and g=9.81 m s^{-2}. With this set of values, B is ~27 GPa and S_S is ~3.6×10^{-7} m^{-1}. Bell (1981) noted a range of values of K for laboratory samples of Dinantian limestone, ranging from 0.07×10^{-9} m s^{-1} to 0.3×10^{-9} m s^{-1}. Lewis et al. (2006) reported much higher values ranging from ~10^{-6} m s^{-1} to ~10^{-2} m s^{-1} in karstified regions. Using the latter set of values, equation (3) gives values for D ranging upward from ~3 m^2 s^{-1}. For comparison, Shepley (2007) determined an upper bound to D for Dinantian limestone in the Peak District of central England by modelling the hydrology of Meerbrook Sough, a disused mine drainage adit that drains a ~40 km^2 area. His analysis reported an upper bound of 50,000 m^2 day^{-1} or ~0.6 m^2 s^{-1}. However, this analysis did not reproduce the observed magnitude of seasonal fluctuations in flow in parts of this subsurface catchment, favouring a higher value of D. Overall, it is inferred that that D ~1 m^2 s^{-1} is appropriate for karstified Dinantian limestone. For comparison, Hornbach et al. (2016) deduced that a poroelastic pressure pulse resulting from large-scale injection of waste water propagated for up to ~40 km through the Ellenburger Formation, a karstified limestone of Ordovician age, in ~6 years, resulting in earthquakes in the vicinity of Dallas,

Texas. Using equation (11) gives an upper bound to D for the Ellenburger Formation of ~1.4 $m^2\ s^{-1}$, in reasonable agreement. Zhang et al. (2013) had previously reported a nominal value of 1 $m^2\ s^{-1}$ for this karstified Ordovician limestone.

Figure 7 here: Graphs of pressure variations

Figure 7(a) illustrates the pressure variations predicted over time, alongside the model seismogenic fault, assuming D=1 $m^2\ s^{-1}$, with ΔP_O=-10 kPa. It indicates that any pressure reduction in this fault will cause significant pressure reductions on short timescales in the surrounding rocks, out to distances of many hundreds of metres.

Notwithstanding the complexity of poroelastic responses in general (e.g., Detournay and Cheng, 1993), the ultimate response following equilibration of pressure between pores and other spaces inside a rock volume is relatively straightforward, and can be expressed as simple proportionality between the change in internal pressure δP and the associated volumetric strain ε,

$$\varepsilon = -\delta P / B \quad , \qquad (13)$$

B being, once again, the 'effective' bulk modulus of the rock (cf. equation (7)). A reduction in internal pressure, as anticipated for the seismogenic fault, will lead to compaction. As the outer ends, away from the fault, of the blocks alongside the fault are 'pinned', compaction will cause their inner ends, facing each other across the fault, to separate slightly, by distance Δx, as depicted schematically in Fig. 5(b).

Since volumetric strain is being assumed, the strain in the x-direction, ε_{xx}, will be $\varepsilon/3$. The quantity Δx defined above can thus be estimated as

$$\Delta x = 2 \int_{x=0}^{x\to\infty} \varepsilon_{xx}\, dx \, , \qquad (14)$$

the factor of 2 taking into account that the rocks on both sides of the fault will move away from it. Likewise, the volume ΔV of water released as a result of this compaction can be estimated as

$$\Delta V = 2\, H\, L \int_{x=0}^{x\to\infty} \varepsilon_{xx}\, dx \, , \qquad (15)$$

where H is the thickness of the Dinantian Limestone and L is the along-strike length of the seismogenic fault.

To evaluate these quantities one needs the integral of erfc(). From Abramowicz and Stegun (1972, p. 299) and Weisstein (2019),

$$E(x) \equiv \int_{z=0}^{z=x} \mathrm{erfc}(z)\, dz = x\, \mathrm{erfc}(x) + \frac{(1 - \exp(-x^2))}{\sqrt{\pi}} \qquad (16)$$

so

$$E(\infty) \equiv \int_{z=0}^{z\to\infty} \mathrm{erfc}(z)\, dz = \frac{1}{\sqrt{\pi}} \qquad (17)$$

Using equation (17), one obtains

$$\Delta x = \frac{-4\, \Delta P_O}{3\, B} \sqrt{\left(\frac{D\, t}{\pi}\right)} \, , \qquad (18)$$

and

$$\Delta V = \frac{-4\, H\, L\, \Delta P_O}{B} \sqrt{\left(\frac{D\, t}{\pi}\right)}\,. \qquad (19)$$

Taking D=1 $m^2\ s^{-1}$, t=1 yr, H=60 m, L=1000 m, ΔP_O=-10 kPa, and B=27 GPa, one obtains Δx=~1.6 mm and ΔV=~280 m^3. For comparison, for an impermeable rock representing basement, with D=0.002 $m^2\ s^{-1}$ (after Zhang et al., 2013) and B=50 GPa, one obtains Δx=~0.04 mm and ΔV=~7 m^3, reflecting the much smaller values of x_M (Fig. 7(b)). The probability of the latter adjustment resulting in separation of asperities (cf. Fig. 5(b)) is much less.

Coulomb failure analysis

The tendency for coseismic slip on the seismogenic fault can be analysed using the standard Coulomb approach. The Coulomb failure parameter Φ:

$$\Phi = \tau - c\,(\sigma_N - P_f)\,, \qquad (20)$$

will thus be evaluated where σ_N, τ and c are the resolved normal stress, shear stress and coefficient of friction on the fault plane, and P_f is the fluid pressure in the fault. Φ=0 marks this condition, with Φ<0 indicating frictional stability under the current state of stress. In general, this condition for shear failure can also be visualized graphically using the standard Mohr circle construction, as a graph of τ against effective normal stress σ_N', defined as $\sigma_N - P_f$ (see below).

Treating the seismogenic fault as having uniform properties throughout its length, the reduction in P_f by ΔP_o will, on its own, act to make the fault more stable. This change in fluid pressure will have no direct effect on τ. The associated reduction in normal stress σ_N can be estimated as $B \times \varepsilon_{xx}$, so will have an effect on Φ that is smaller in magnitude than the direct effect of the decrease in P_f. Overall these considerations lead to the conclusion that a reduction in fluid pressure in a fault will 'clamp' the fault, increasing its stability. This is in accordance with the widespread observation that increases in P_f can 'unclamp' or destabilize faults, this being the accepted mechanism for the widespread occurrence in recent years of seismicity caused by fluid injection (e.g., Ellsworth, 2013; Keranen et al., 2014; Walsh and Zoback, 2015; Weingarten et al., 2015). On this basis, one might conclude that a decrease in the groundwater pressure within the seismogenic fault cannot be the cause of the Newdigate seismicity.

However, it is generally accepted that the mechanics of faults, notably whether they are stable or can slip seismically, are determined by the properties of strong patches – asperities – where the opposite surfaces of the fault are in frictional contact (e.g., Reiter, 1999). A fault surface consisting, on a microstructural scale, of a fractal size distribution of asperities with a small proportion of the fault surface in contact, in proportion to the normal stress applied to the fault, can mimic the effect, on a macroscopic scale, of a constant coefficient of friction (e.g., Archard, 1957; Mitchell et al., 2012). Brown and Scholz (1985) showed that natural rock surfaces follow fractal scaling for surface features of height up to ~0.1 m. Laboratory simulations of faulting often include asperities on a microstructural scale, occupying only a small proportion of the overall area of a fault (e.g., Harbord et al., 2017; Selvadurai and Glaser, 2017). Most recently, the view has gained ground that the physics of co-seismic faulting is likewise governed by processes on a microstructural scale (e.g., Acosta et al., 2017; McDermott et al., 2017). For example, McDermott et al. (2017) deduced that asperities can be patches of fault with areas of no more than a few square metres, their properties being determined by mineral grains with dimensions of microns. Because these strong patches with fault surfaces in contact occupy only a small proportion of a fault surface, they act as stress concentrations. For example, in the laboratory experiments by Selvadurai and Glaser (2017), millimetre-sized asperities with micron-sized heights occupy a very small proportion of the fault area; in one experimental run, a decrease in the mean normal stress across the fault area by ~0.3 MPa caused decreases in the normal stress affecting individual asperities by ~10 MPa.

Figure 5(b) illustrates how a small increase in separation of fault surfaces, Δx, can destabilize a fault through its effect on the extent of contact between asperities. Moving from configuration (i) to configuration (ii), two of the three asperities depicted will no longer contribute to fault stability. The third one will experience a significantly reduced normal stress, as a result of the increased separation of the fault surfaces. This will reduce the maximum shear stress that this asperity can sustain, in accordance with equation (20), whereas the shear stress that it is required to sustain to keep the fault stable will increase because the other asperities no longer contribute. Overall, it can thus be seen how a small increase in separation of fault surfaces might bring a fault significantly closer to the condition for slip, and might indeed result in coseismic slip.

Figure 8 here: Mohr circle diagrams

The geomechanical consequences of this model can now be illustrated using the standard Mohr circle construction (Fig. 8). In the absence of more definitive data (see the online supplement), a model stress field is adopted (based on analysis of the Preese Hall case study) at 2400 m depth from Westaway (2017) with σ_H=63.3 MPa, σ_V=54.3 MPa, and σ_h=39.2 MPa, with hydrostatic groundwater pressure P_f=23.5 MPa. A typical orientation is adopted for a patch of the seismogenic fault of strike 270°, dip 80° and rake 170° (cf. Table 3). Analyzing these values using the same software as was used for the Westaway (2017) analysis of Preese Hall (and for analysis of the Pohang case study by Westaway and Burnside, 2019), the optimum azimuth of the maximum principal stress is determined as 300° (or N60°W-S60°E), which predicts a rake of 150°. This differs from the observed rake of 170°, indicating that the assumed model stress field is not quite right for the present study area. This mismatch could be reconciled by adjustments to the magnitudes of the principal stresses or by incorporating inclined principal stresses, but in the interests of brevity such refinements are omitted here. Subject to this proviso, Fig. 8(a) indicates that the model stress field indicates Φ ~-2 MPa relative to a standard frictional failure threshold with c=0.6, the model normal and shear stresses across the fault being 21.4 and 10.6 MPa. The depicted state of stress on the seismogenic fault represents the average conditions across the fault; in reality, stability of this fault was maintained at asperities, probably occupying a small proportion of the fault area, at which the normal and shear stresses were much higher than the depicted average values.

In contrast, Figure 8(b) sets out to represent the conditions at the point of coseismic slip. It takes into account the inferred 10 kPa reduction in fluid pressure in the fault. It represents the effect of compaction of the Dinantian limestone reducing the number of asperities in contact and thus affecting the normal and shear stresses on the remaining asperities. Thus, the model σ_H has been increased by ~1.8 MPa and the model σ_h has been decreased by ~2.4 MPa, causing an increase in the model shear stress across the fault to 12.2 MPa and decreasing the model normal stress across it to ~20.3 MPa and bringing the model fault to the Coulomb condition for slip. Following the reasoning of Mitchell et al. (2013), this ~4% reduction in normal stress is interpreted as a consequence of a ~4% reduction in the proportion of the fault surface that is in frictional contact, as a result of the compaction of the adjoining rocks caused by their loss of fluid pressure.

Discussion

The proposed mechanism for the Newdigate seismicity depends on a pressure drop within the Dinantian limestone alongside the seismogenic strand of the Newdigate fault zone, as a result of depressurization of the groundwater within this fault. A simple approach to mitigation, albeit at considerable cost, would be to provide an injection well in or near this fault to replace the lost groundwater and thereby balance the groundwater pressure in and around the fault. It follows from the present analysis that if the approved plans for more wells at Horse Hill proceed, with much higher

production rates than for HH1, the pressure drawdown in the seismogenic fault will increase and – in the absence of the aforementioned mitigation - seismicity might recur.

In principle, testing of the proposed mechanism is possible, since the inferred volumetric strain implies vertical as well as horizontal compaction. Hicks et al. (2019) considered this aspect, concluding on the basis of other cases studies known to them that there was no precedent for strike-slip earthquakes to be caused by compaction. There is, however, no geomechanical reason why compaction cannot cause strike-slip earthquakes, if the compaction occurs in a region such as the Weald Basin where the stress field favours this mechanism. The predicted vertical compaction will result in subsidence of the Earth's surface, and so is in principle observable; its magnitude can be calculated as an integration similar to that for equation (14); for the parameter values already discussed, including the estimated ~60 m thickness of the Dinantian limestone, it will be a small fraction of 1 mm. Multiple techniques, including interferometric synthetic-aperture radar (InSAR) and repeated gravity and GPS measurements, can in principle measure vertical crustal motions such as this. A combined dataset of this type has been analysed for a region of southeast England, including the northern Weald Basin, by Aldiss et al. (2014). At the October 2018 workshop attention was also drawn to an InSAR-derived surface deformation map of Britain by GVL (2018), spanning October 2015 to October 2017. The Aldiss et al. (2014) analysis revealed vertical crustal motions at ~1 mm a^{-1}, caused by processes such as extraction of groundwater (or replenishment of groundwater reservoirs previously depleted by extraction). Such rates make it impossible to resolve the much smaller changes expected from compaction of the Dinantian limestone at Newdigate.

Much has been made by participants in the OGA (2018) workshop regarding the extent to which the Newdigate earthquake 'swarm' might fit the standard criteria identified by Davis and Frohlich (1993) for establishing whether instances of seismicity are anthropogenic (e.g., Baptie and Luckett, 2018). UKOG (2019a) have argued that this set of criteria is inapplicable as they relate to seismicity caused by fluid injection, which is not the causal mechanism in this case. However, familiarity with the literature in this field (e.g., Foulger et al., 2018) indicates that these criteria are widely used irrespective of the geomechanical cause of any particular anthropogenic earthquake. Verdon et al. (2019) proposed a different approach to assessing anthropogenic seismicity. This approach appears problematic, since it replaces the objective (yes / no) criteria recommended by Davis and Frohlich (1993) with subjective numerical scores. The development of a conceptual geomechanical model for the Newdigate earthquakes supersedes the other Davis and Frohlich (1993) criteria; nonetheless, an appraisal of this seismicity in terms of these criteria is included in the online supplement.

While preparation of this text was under way, it was announced in December 2019 that well HH2Z was experiencing significant water ingress, at rates approaching 1 l s^{-1}, from a fracture near the 'toe' of its horizontal section (UKOG, 2019c); during early 2020 this well toe was plugged to stop this ingress (UKOG, 2020a, 2020b). This instance indicates significant fracture permeability, as is required by the proposed conceptual model (Fig. 5).

Furthermore, also while text preparation was under way, OGA (2019) released details of the largest earthquake caused by 'fracking' of well Preston New Road-2 near Blackpool in northwest England. This event, of M_L 2.9, occurred at 07:30 on 26 August 2019 at a depth reported by BGS as 2.5 km; the resulting peak ground velocity of 8 mm s^{-1} is broadly consistent with what is inferred for the largest Newdigate events in the present study (see the online supplement). This M_L 2.9 event resulted, on 1 November 2019, in the imposition by the UK government of a moratorium on 'fracking' in England, superseding the previous regulation that earthquakes of M_L<0.5 were 'allowed'. This has created a strange regulatory situation where 'fracking' is forbidden on the basis of seismicity but there is no regulatory limit for seismicity caused by other technologies (such as conventional hydrocarbon production or, indeed, development of geothermal energy projects). It is suggested that a consistent

approach is needed, maybe based on the established procedure for regulating other forms of industrial nuisance vibration (cf., Westaway and Younger, 2014).

The remainder of this discussion will concentrate on geomechanical issues. Following each of the Newdigate earthquakes, the spatially averaged shear stress on the patch of fault that slipped will reduce by a value equal to the coseismic stress drop $\Delta\sigma$, moving the state of stress away from the Coulomb failure condition. However, if groundwater withdrawal from the Dinantian limestone continues, the possibility exists that the fault will ultimately adjust once again towards the failure condition by repetition of the same physical mechanism. Ultimately, maybe after multiple earthquake cycles, one can envisage so much previously stored elastic strain energy being released from the vicinity of the seismogenic fault that the activity eventually dies out. This mechanism might thus explain the decline in earthquake activity in the latter part of 2019 (Table 4), even though oil production has continued (and, indeed, its rate increased following the completion of well HH2Z). It is thus of interest to consider whether the existing dataset provides evidence for repeated slip on the same patches of fault; this aspect is now considered.

To investigate the area of the patch of fault that slipped in each earthquake, seismic moment M_O is first determined from magnitude M_W using the standard formula

$$\log_{10}(M_o / \text{N m}) = 9.05 + 1.5\, M_W \qquad (21)$$

(Hanks and Kanamori, 1979). For most of the Newdigate earthquakes, M_W values are unavailable from the Hicks et al. (2019) dataset; M_L is used as a proxy for M_W. Next, the radius a of the equivalent circular seismic source is determined from M_o, assuming a nominal value of the coseismic stress drop $\delta\sigma$:

$$M_o = \frac{16\, \delta\sigma\, (1 - \nu)\, a^3}{3\, (2 - \nu)} \qquad (22)$$

(e.g., Westaway and Younger, 2014), where ν is Poisson's ratio for the adjoining rock volume. The source area A is then determined as $\pi\, a^2$ and the mean slip u as $M_o / (\mu\, A)$. The value of μ comes from the standard formula $\mu \equiv 3\, B\, (1 - 2\, \nu) / (2(1 - \nu))$. For Dinantian limestone ν ranges between 0.19 and 0.31 (Bell, 1981) so 0.25 is adopted, for which $\mu \equiv B$; as before B=50 GPa, from Bell (1981).

This task was carried out for the complete Hicks et al. (2019) earthquake dataset, plus the additional events listed in Table 4. The cumulative seismic moment thus obtained was ~1.5×10^{14} N m, equivalent to a single earthquake of M_W ~3.4. Assuming $\delta\sigma$=10 MPa, a plausible upper bound, the cumulative area of fault rupture is estimated as ~2.1×10^5 m^2 and the mean coseismic slip in the largest earthquake as ~2.2 cm. Taking 2 km as an upper bound to the length of the seismogenic zone, from Fig. 1, and 60 m as the thickness of the Dinantian limestone, the area of fault in this lithology is ~1.2×10^5 m^2. Calculated on this basis, the total area of coseismic ruptures exceeds the area of the fault, and would be even greater if a lower value of $\delta\sigma$ were to be assumed. Thus, either patches of fault slipped more than once, or that the seismicity propagated into the overlying and/or underlying lithologies, although the 'cloud' of hypocentres located by Hicks et al. (2019) indicates no clear propagation in any direction. The calculations also indicate that the eight largest earthquakes have source diameters larger than the estimated 60 m thickness of the limestone; evidently, these events either ruptured outside this layer or ruptured patches of fault that are elongated horizontally. Assuming the latter explanation, and that the overall population of earthquakes was distributed to produce a constant overall amount of coseismic slip across the fault, this amount is determined as ~2.5 cm, roughly as estimated for the largest individual earthquake. It is thus possible that the earthquake swarm was indeed 'self-limiting', and that once the full extent of the seismogenic fault had slipped by this distance, the fault was effectively 'de-stressed' and the activity died out, consistent with its observed cessation in late 2019 (Table 4). Further analysis of this aspect is evidently warranted, given the possibility that seismicity

might resume, as a result of pressure changes arising from the planned increase in production at the Horse Hill site.

As already noted, the proposed physical mechanism, whereby a decrease in the fluid pressure within a fault can destabilize the fault, is the opposite of what might be termed the 'usual' effect, the unclamping that will occur when the fluid pressure within a fault increases and causes the effective normal stress to reduce. The present analysis depends on the poroelastic compaction effect that will also occur within the rocks adjoining the fault, which is shown to be capable of causing separation of the fault surfaces by a distance of the order of 1 mm in the highly permeable Dinantian limestone, plus the inference that the characteristic height of asperities on fault surfaces in this lithology is less than this increase in separation, so the state of stress on these asperities is significantly affected. It is suggested that in these unusual circumstances, where a permeable fault occurs in permeable rocks, this poroelastic effect can outweigh the 'usual' effect whereby a decrease in fluid pressure would lead to increased fault stability.

Although fluid injection is nowadays recognized as a widespread cause of induced seismicity, it is worth noting that reductions in fluid pressure caused by fluid extraction has been linked to seismicity for far longer. The first instance recognized is by Pratt and Johnson (1926), for earthquakes accompanying oil production near Houston, Texas. Other case studies subsequently recognized include those by Calloi et al. (1956), Kovach (1974), Rothé and Lui (1983), Simpson and Leith (1985), Pennington et al. (1986), Wetmiller (1986), Grasso and Wittlinger (1990), Doser et al. (1991), Ottemöller et al. (2005), Dahm et al. (2015), and Hornbach et al. (2015), whereas works discussing physical mechanisms for such seismicity include those by Yerkes and Castle (1976), Simpson et al. (1988), Segall (1989), and Segall and Fitzgerald (1998). Hornbach et al. (2015) indeed considered a complex case study, at Azle near Fort Worth, Texas, where earthquake activity began in 2013 in a locality that had experienced both injection (of industrial wastewater) and production (of brine, oil and natural gas). The injection was initially suspected as the cause, on account of its very large volume, but the Hornbach et al. (2015) analysis indicates the pressure reduction caused by oil and gas production as the most important individual factor. Some of the above works (e.g., Pennington et al., 1986) have recognized the significance of processes required in the present conceptual model (e.g., compaction of limestone and failure of asperities), and others (e.g., Holland, 2013; Schultz et al., 2015; Igonin et al., 2019) have recognized that highly permeable connections can cause seismicity at significant distance from the source of the causative change in fluid pressure. However, no previous case study known to the present author has proposed a geometry between the source of depressurization and the seismogenic fault that resembles this conceptual model (Fig. 5).

The 'usual' effect of an increase in fluid pressure causing fault unclamping is to be expected if the fault is in impermeable rocks, where the fluid pressure only acts within the fault and not within the adjoining rock volume (e.g., Hackston and Rutter, 2016; Westaway, 2017). If the rock volume has zero permeability there will be no poroelastic effect. If it has very low permeability, increased pressure in an adjoining fault will increase the fluid pressure in it, which will dilate the volume and, on a microstructural scale, increase the contact area of asperities, partly cancelling the direct effect of the pressure increase. Conversely, if the rock volume has high permeability, increased pressure in an adjoining fault might cause sufficient poroelastic dilatation of the rock volume and so increase the contact area of asperities, such that, overall, the fault experiences net clamping. In general, for faults within permeable rocks, one can expect these two effects to counteract each other; whether the microscopic effect of asperities will predominate or not will depend on the conditions in each case. In this context, it is noteworthy that much of the seismicity associated with fluid injection in the USA occurs as a result of pressure increases in faults in impermeable basement rocks, rather than in the permeable rocks into which the injection takes place, an example being the case study documented by Hornbach et al (2015) (see also, e.g., Kim et al., 2013, and Zhang et al., 2013). In other instances,

for example that discussed by Justinic et al. (2013), authors have emphasised the proximity of hypocentres to injection points to highlight the possibility of a human cause, when many hypocentres are in fact rather deeper and indicate earthquakes within the underlying impermeable basement. Hincks et al. (2018) have noted that fluid injection into faults or fractures in basement or near the contact with basement at the base of permeable sediments is statistically much more likely to result in seismicity than injection well above basement. Consideration of poroelasticity provides an explanation for this empirical observation.

It has been argued (OGA, 2018) that the Brockham and Horse Hill wells are not hydraulically connected as pressure variations imposed in one are not seen in the other. However, due to the separation of these wells (~8 km; Fig. 1) and the finite hydraulic diffusivity of the intervening rocks, one would not expect instantaneous correlation. Given equation (11), with R=8 km, the approximate distance from well BRX2Y to the Newdigate seismicity cluster, D=1 $m^2 s^{-1}$ would make t_D ~4 months; D=20 $m^2 s^{-1}$ would make t_D ~6 days. With R=4 km, the approximate distance from HH1, D=1 $m^2 s^{-1}$ would make t_D ~1 month; D=20 $m^2 s^{-1}$ would make t_D ~1.5 days. Given these distances, the observed time lags between the starts of production and starts of seismicity of 9 days for well BRX2Y and 3 days for well HH1 indicate D=14 $m^2 s^{-1}$ and D=10 $m^2 s^{-1}$, respectively. No study, known to the present author, has looked for any correlation of the seismicity with the sequence of activities (and associated pressure variations) at either well assuming these or any other duration of time lag. The pressure data that might demonstrate or refute any such correlation are not in the public domain.

In the absence of more detailed information, it is assumed (to calculate an upper bound to the pressure reduction) that the initial ~4 m^3 of oil obtained from well BRX2Y in March 2018 was produced from the wellbore, with no flow from the reservoir, possibly because of previous development of water coning around the production interval. Assuming well casing with an 8.625 inch external diameter and a 7.435 inch or 188.85 mm internal diameter, a standard size, ~4 m^3 of production would reduce the oil level within the well by ~140 m and thus reduce the pressure at the base of this oil column by ~1 MPa. The average pressure reduction ΔP_P during this production would thus be ~0.5 MPa. On the following day, the well was shut in, then on 25 March water injection (into well BRX3) was started, which led to some additional production (Hicks et al., 2019; Fig. 1). Taking Δt for the pressure transient as 8 hours (a working shift at the well site), and ΔP_P=0.5 MPa, with r=8 km and D=14 $m^2 s^{-1}$, equation (12) gives $\delta P_M \cong 3$ kPa. On reaching the patch of the seismogenic fault within the Dinantian limestone, such a pressure perturbation would act to unclamp the fault, in accordance with earlier discussion, potentially accounting for the start of the seismicity on 1 April 2018.

Clearly this is a very crude calculation: it does not incorporate the 2-D geometrical spreading that would be expected for a pressure transient within the calcite 'beef' fabric in the Portland sandstone, which would reduce the pressure perturbation at a given distance. On the other hand, it could be argued from the record of activity at Brockham (see online supplement) that the assumed duration of this transient should exceed ~8 hours, which would increase the predicted value of δP_M. It is suggested that subsequent production from the Portland sandstone at both BRX2Y and HH1 will cause additional pressure perturbations within the seismogenic fault, causing later seismicity, but their effect is not amenable to analytic calculations and will require numerical modelling. Once BRX2Y production ended, the good correlation between seismicity and production from the Portland reservoir at HH1 (Fig. 4(c)) supports the proposed explanation and is consistent with t_D being quite short, implying a high value of D and supporting the inference that this is based on the high permeability and hydraulic conductivity of calcite 'beef'. The net result of these pressure perturbations will be flow transients from the seismogenic fault towards the wells, superimposed on the pre-existing flow towards well BRX2Y, already discussed. It is suggested that these flow transients will be maintained by outflow of groundwater from, and compaction of, Dinantian limestone adjoining this fault.

A permeability of ~1 D in calcite 'beef' would correspond, given equation (4), for water with a viscosity of ~0.9 mPa s (appropriate for ~25 °C, as expected locally at ~600 m depth; e.g., Busby et al., 2011) to K ~1.1×10^{-5} m s^{-1}. From equation (3), with specific storage S_S ~10^{-6} m^{-1}, a hydraulic diffusivity of ~11 m^2 s^{-1} can be determined, roughly as required for the proposed conceptual model to be feasible. Furthermore, the analysis has indicated estimated production of ~300 m^3 of water from the Dinantian limestone into the seismogenic fault during the course of a year, as a result of ~4700 m^3 of production from the Portland reservoir at HH1. Evidently, most of the groundwater flow to balance this production came from elsewhere. The associated time-averaged volume flow rate is thus ~10^{-5} m^3 s^{-1} or ~0.01 l s^{-1}. If sustained across a width of ~1 km (the along-strike length, estimated earlier, of the seismogenic fault) in a ~5 m thick layer of calcite 'beef', this would indicate a mean flow velocity of ~2×10^{-9} m s^{-1}. From equation (5) this would indicate a flow-parallel pressure gradient of ~2 Pa m^{-1}, which would require a pressure drop of ~8 kPa over ~4 km distance. To sustain this pressure drop plus the estimated 10 kPa pressure drop within the Dinantian limestone requires a time-averaged pressure decrease in the Portland reservoir at Horse Hill of at least ~18 kPa, a small proportion of the maximum pressure drop that has been reported. Modest pressure changes of this order, which might well be expected as a result of oil production, demonstrate the feasibility, in principle, of the proposed geomechanical model. Notwithstanding the repetition, it is noted again that availability of pressure data would facilitate testing of this model.

Conclusions

The seismicity at Newdigate, Surrey, during 2018-2019, has been reassessed, amending aspects where the Hicks et al. (2019) analysis has proved inaccurate. First-order correction for the seismic velocity model that they used for earthquake location, which was too slow for the local stratigraphy, adjusts the hypocentres ~400 m deeper than previously thought, to depths of ~2400 m, placing them within the Palaeozoic 'basement' beneath the Weald Basin rather than within its Jurassic sedimentary sequence. These earthquakes involved mainly right-lateral slip on a steeply north dipping fault, part of the Newdigate fault zone (Fig. 2).

Oil was produced during 2018-2019 in this vicinity from two wells in the Upper Portland Sandstone reservoir, Brockham-X2Y and Horse Hill-1. Previous workers, including Hicks et al. (2019), have dismissed the possibility that activity affecting these wells has caused the Newdigate seismicity. However, the correlation between phases of production from this reservoir and 'clusters' of earthquake activity (Fig. 4) is compelling, and warrants consideration of potential geomechanical mechanisms. A conceptual model that can account for this cause an effect connection is indicated schematically in Fig. 5. It is thus suggested that the seismicity occurred within a thin (estimated ~60 m thick) layer of permeable Dinantian limestone, which is hydraulically connected to the Portland reservoir via permeable strands of the Newdigate fault zone and by the highly permeable calcite 'beef' fabric within the Portland sandstone. It is hypothesized that past oil production at Brockham depressurized the Portland reservoir around this well and drew groundwater from the Dinantian limestone, causing it to compact and 'unclamp' the seismogenic fault but not sufficiently to reach the Coulomb failure criterion to initiate seismicity. The resumption of production at Brockham in March 2018 caused a negative pressure pulse to propagate through the hydraulic connection to the Dinantian limestone, which reached the failure threshold, initiating the first 'cluster' of Newdigate seismicity in April 2018. Likewise, a negative pressure pulse following resumption of production from the Portland reservoir at Horse Hill in February 2019 initiated a subsequent 'cluster' of seismicity. This mechanism requires hydraulic diffusivity ~10 m^2 s^{-1} in the calcite 'beef' and ~1 m^2 s^{-1} in the Dinantian limestone. At other times, the complexity of production patterns (from both BRX2Y and HH1 in summer 2018 and multiple suspensions of production from HH1 during 2019) and the absence of pressure data prevent any detailed conclusions being drawn, although the general correlation of seismicity with production from the Portland reservoir (Fig. 4) is compelling. The proposed 'unclamping' effect requires consideration of the fractal nature of asperities on the seismogenic fault and their response to

compaction of the adjoining limestone. Such behaviour, previously unrecognized in studies of seismicity caused by fluid extraction, is particularly significant in this instance because of the high permeability of the Dinantian limestone; in impermeable rocks a reduction in pore pressure would cause fault clamping rather than unclamping. In principle this model is testable, but required data, notably the history of pressure variations in the oil wells, is not currently in the public domain.

The recognition that this instance of seismicity is arguably caused by human activity, and the role of highly permeable hydraulic connections extending for many kilometres, has significant implications for regulation to mitigate the potential nuisance from future seismicity caused by oil production in the Weald Basin, and may well also help to inform the understanding of anthropogenic seismicity in other settings. The initial response to the Newdigate seismicity, which included claims that any connection with oil production was implausible before any geomechanical analysis had been done, was inappropriate.

Acknowledgements
Imagery and metadata for seismic line TWLD-90-15 were kindly provided by Malcolm Butler from the UK Onshore Geophysical Library / 'Beneath Britain' archive.

References – for both manuscript and supplement (will be rationalized later)

Abramowitz, M., Stegun, I.A., 1972. Handbook of Mathematical Functions with Formulas, Graphs, and Mathematical Tables, 10th ed. Dover, New York, 1040 pp.

Acosta, M., Passelègue, F.X., Schubnel, A., Violay, M., 2018. Dynamic weakening during earthquakes controlled by fluid thermodynamics. Nature Communications, 9, 3074, 9 pp., doi: 10.1038/s41467-018-05603-9

Agosta, F., Prasad, M., Aydin, A., 2007. Physical properties of carbonate fault rocks, Fucino Basin (central Italy): implications for fault seal in platform carbonates. Geofluids, 7, 19–32.

Aldiss, D., Burke, H., Chacksfield, B., Bingley, R., Teferle, N., Williams, S., Blackman, D., Burren, R., Press, N., 2014. Geological interpretation of current subsidence and uplift in the London area, UK, as shown by high precision satellite-based surveying. Proceedings of the Geologists' Association, 125, 1–13.

Al Duhailan, M.A., Sonnenberg, S.A., 2014. The curious case of hydrocarbon-expulsion fractures: Genesis and impact on the Bakken Shales. Search and Discovery, 80398, 30 pp.

Al Duhailan, M.A., Sonnenberg, S.A., Longman, M., 2015. Analyzing beef fractures: Genesis and relationship with organic-rich shale facies. SPE Unconventional Resources Technology Conference, 20-22 July 2015, San Antonio, Texas, paper URTEC-2151959-MS, doi: 10.15530/URTEC-2015-2151959

Allen, D.J., Brewerton, L.J., Coleby, L.M., Gibbs, B.R., Lewis, M.A., MacDonald, A.M., Wagstaff, S.J., Williams, A.T., 1997. The physical properties of major aquifers in England and Wales. British Geological Survey Technical Report WD/97/34, 312 pp. Environment Agency R&D Publication 8. http://nora.nerc.ac.uk/id/eprint/13137/1/WD97034.pdf

Andrews, I.J., 2014. The Jurassic shales of the Weald Basin: geology and shale oil and shale gas resource estimation. British Geological Survey for Department of Energy and Climate Change, London, UK, 79 pp.

Angus Energy, 2018a. OGA – Surrey earthquakes. https://www.ogauthority.co.uk/media/5160/7c-angus-maps-for-oga-meeting.pdf

Angus, 2018. Brockham Portland & Kimmeridge Reservoirs. Addendum to the Field Development Plan. Angus Energy, Plc., London, 32 pp. https://www.whatdotheyknow.com/request/523935/response/1277768/attach/4/brockfdpadd%20Redacted.pdf?cookie_passthrough=1 (partly redacted version released under a Freedom of Information request)

Archard, J.F., 1957. Elastic deformation and the laws of friction. Proceedings of the Royal Society of London, Series A, Mathematical and Physical Sciences, 243, 190–205.

Baptie, B., 2006. UK Earthquake Monitoring 2005/2006. British Geological Survey, Nottingham. http://www.earthquakes.bgs.ac.uk/publications/annual_reports/2006_17th_annual_report.pdf

Baptie, B., Luckett, R., 2018. The Newdigate earthquake sequence, 2018. British Geological Survey Internal Report OR/18/059, 20 pp. https://earthquakes.bgs.ac.uk/research/NewdigateEarthquakesReport.pdf

Barton, C.A., Zoback, M.D., Moos, D., 1995. Fluid flow along potentially active faults in crystalline rock. Geology, 23, 683–686.

Bayerly, M., Brooks, M., 1980. A seismic study of deep structure in South Wales using quarry blasts. Geophys. J. R. astr. Soc. 60, 1-19.

BBC, 2018. Seventh tremor strikes in Surrey 'quake swarm'. British Broadcasting Corporation, London. https://www.bbc.co.uk/news/uk-england-44727326

BBC, 2019a. 'Surrey swarm' quakes 'not caused by oil extraction'. British Broadcasting Corporation, London. https://www.bbc.co.uk/news/uk-england-surrey-49480365

BBC, 2019b. Horse Hill: Oil drilling to expand in Surrey countryside. British Broadcasting Corporation, London. https://www.bbc.co.uk/news/uk-england-surrey-49665269

Bell, F.G., 1981. A survey of the physical properties of some carbonate rocks. Bulletin of the International Association of Engineering Geology, 24, 105–110.

Bense, V.F., Gleeson, T., Loveless, S.E., Bour, O., Scibek, J., 2013. Fault zone hydrogeology. Earth-Science Reviews, 127, 171–192.

Bisdom, K., Baud, E., Estrada, S., Sanz-Perl, Y., Gauthier, B., Bertotti, G., 2016. Coupled stress-fluid pressure modelling of stimulated rock volume in shale - impact of natural fractures and beef. 78th EAGE Conference and Exhibition, Vienna, Austria, 30 May - 2 June 2016. doi: 10.3997/2214-4609.201601164

Blake, D., Mlisa, A., Hartnady, C., 2010. Large scale quantification of aquifer storage and volumes from the Peninsula and Skurweberg Formations in the southwestern Cape. Water SA, 36 (2), 177-184.

Bommer, J.J., Dost, B., Edwards, B., Kruiver, P.P., Ntinalexis, M., Rodriguez-Marek, A., Stafford, P.J., van Elk, J., 2017a. Developing a model for the prediction of ground motions due to earthquakes in the Groningen gas field. Netherlands Journal of Geosciences, 96 (5), S203–S213.

Bommer, J.J., Stafford, P.J., Edwards, B., Dost, B., van Dedem, E., Rodriguez-Marek, A., Kruiver, P., van Elk, J., Doornhof, D., Ntinalexis, M., 2017b. Framework for a ground-motion model for induced seismic hazard and risk analysis in the Groningen gas field, the Netherlands. Earthquake Spectra 33, 2, doi: 10.1193/082916EQS138M.

Bommer, J.J., Stafford, P.J., Ntinalexis, M., 2017c. Empirical Ground-Motion Prediction Equations for Peak Ground Velocity from Small-Magnitude Earthquakes in the Groningen Field Using Multiple Definitions of the Horizontal Component of Motion. Updated Model for Application to Smaller Earthquakes. Nederlandse Aardolie Maatschappij BV, Assen, The Netherlands, 23 pp. https://nam-feitenencijfers.data-app.nl/download/rapport/62551a04-c1c3-4712-86e8-6c625ab5ee4c?open=true

Bond, C.E., Gibbs, A., Shipton, Z.K., Jones, S., 2007. What do you think this is? "Conceptual uncertainty" in geoscience interpretation. GSA Today, 17 (11), 4–10.

Brown, S.R., Scholz, C.H., 1985. Broad bandwidth study of the topography of natural rock surfaces. Journal of Geophysical Research, 90, 12,575-12,582.

Buckland, W., De la Beche, H.T., 1835. On the geology of the neighbourhood of Weymouth and the adjacent parts of the coast of Dorset. Transactions of the Geological Society, London, Series 2, 4, 1-46.

Busby, J., Kingdon, A., Williams, J., 2011. The measured shallow temperature field in Britain. Quarterly Journal of Engineering Geology and Hydrogeology, 44, 373–387.

Busby, J.P., Smith, N.J.P., 2001. The nature of the Variscan basement in southeast England: evidence from integrated potential field modelling. Geological Magazine, 138, 669–685.

Butler, M., Pullan, C.P., 1990. Tertiary structures and hydrocarbon entrapment in the Weald Basin of southern England. In: Hardman, R.F.P., Brooks, J. (eds), Tectonic Events Responsible for Britain's Oil and Gas Reserves. Geological Society, London, Special Publications, 55, 371-391.

Caine, J.S., Evans, J.P., Forster, C.B., 1996. Fault zone architecture and permeability structure. Geology, 24, 1025-1028.

Calloi, P., DePanfilis, M., DeFilippo, D., Marcelli, L., Spadea, M.C., 1956. Terrimoti della Val Padana del 15-16 Maggio 1951. Annali di Geofisica, 9, 63-105 (with summary in English).

Carey, J.W., Lei Zhou, Rougier, E., Mori, H., Viswanathan, H., 2015. Fracture-permeability behavior of shale. Journal of Unconventional Oil and Gas Resources, 11, 27-43.

Cavanagh, A., Gilfillan, S., Haszeldine, S., 2019. Further potential for earthquakes from oil exploration in the Weald. https://www.keithtaylormep.org.uk/sites/default/files/download/2019-02/Newdigate%20Short%20Summary%20Edinburgh%20Uni%20Feb%202019.pdf

Chadwick, R.A., 1986. Extension tectonics in the Wessex Basin, southern England. Journal of the Geological Society, London, 143, 465-488.

Chadwick, R.A., Kenolty, N., Whittaker, A., 1983. Crustal structure beneath southern England from deep seismic reflection profiles. Journal of the Geological Society, London, 140, 893-911.

Chadwick, R.A., Pharaoh, T.C., Williamson, J.P., Musson, R.M.W., 1996. Seismotectonics of the UK. British Geological Survey Technical Report, WA/96/3C. British Geological Survey, Keyworth, Nottingham, 172 pp. Available online: http://core.ac.uk/download/pdf/59774.pdf

Cobbold, P.R., Rodrigues, N., 2007. Seepage forces, important factors in the formation of horizontal hydraulic fractures and bedding-parallel fibrous veins ('beef' and 'cone-in-cone'). Geofluids, 7, 313–322.

Cobbold, P.R., Zanella, A., Rodrigues, N., Løseth, H., 2013. Bedding-parallel fibrous veins (beef and cone-in-cone): Worldwide occurrence and possible significance in terms of fluid overpressure, hydrocarbon generation and mineralization. Marine and Petroleum Geology, 43, 1-20.

Costain, J.K., 2017. Groundwater recharge as the trigger of naturally occurring intraplate earthquakes. In: Landgraf, A., Kübler, S., Hintersberger, E., Stein, S. (eds), Seismicity, Fault Rupture and Earthquake Hazards in Slowly Deforming Regions. Geological Society, London, Special Publications, 432, 91–118.

Cuadrilla, 2019. Preston New Road-1z: LJ/06-09(z) HFP Report. Cuadrilla Bowland Ltd., Preston, 25 pp. https://www.ogauthority.co.uk/media/5845/pnr-1z-hfp-report.pdf

Dahm, T., Cesca, S., Hainzl, S., Braun, T., Krüger, F., 2015. Discrimination between induced, triggered, and natural earthquakes close to hydrocarbon reservoirs: A probabilistic approach based on the modeling of depletion-induced stress changes and seismological source parameters. Journal of Geophysical Research, 120, 2491–2509.

Dake, L.P., 1998. Fundamentals of Reservoir Engineering. Developments in Petroleum Science series, volume 8, 17th edition. Elsevier, London, 498 pp.

Davies, R., Foulger, G., Bindley, A., Styles, P., 2013. Induced seismicity and hydraulic fracturing for the recovery of hydrocarbons. Marine and Petroleum Geology, 45, 171–185.

Davis, S.D., Frohlich, C., 1993. Did (or will) fluid injection cause earthquakes? - Criteria for a rational assessment. Seismological Research Letters, 64 (3-4), 207-224.

DECC, 2013. The Hydrocarbon Prospectivity of Britain's Onshore Basins. Department of Energy and Climate Change, London, 93 pp. https://www.ogauthority.co.uk/media/1695/uk_onshore_2013.pdf

Detournay, E., Cheng, A.H.-D., 1993. Fundamentals of poroelasticity. Chapter 5 in C. Fairhurst (ed.) Comprehensive Rock Engineering: Principles, Practice and Projects, Vol. II, Analysis and Design Method. Pergamon Press, Oxford, pp. 113-171.

De Wiest, R.J.M., 1966. On the storage coefficient and the equations of groundwater flow. Journal of Geophysical Research, 71, 1117-1122.

Dines, H.G., Edmunds, F.H., 1933. The geology of the country around Reigate and Dorking: memoir for 1:63,360 geological map sheet 286 (England and Wales). H.M.S.O., London, 204 pp.

Doser, D.I., Baker, M.R., Mason, D.B., 1991. Seismicity in the War-Wink gas field, Delaware Basin, West Texas, and its relationship to petroleum. Bulletin of the Seismological Society of America, 81, 971-986.

Ellsworth, W.L., 2013. Injection-induced earthquakes. Science, 341, 1225942, 7 pp. doi: 10.1126/science.1225942.

Europa, 2004. Application for Production Licence. Appendix B – Geotechnical Information. Europa Oil & Gas Ltd., London, 38 pp. https://ukogl.org.uk/map/php/pdf.php?subfolder=industry_reports&filename=41436.pdf

Evans, C.J., Brereton, N.R., 1990. *In situ* crustal stress in the United Kingdom from borehole breakouts. In: Hurst, A., Lovell, M.A., Morton, A.C. (eds), Geological Applications of Wireline Logs. Geological Society, London, Special Publications, 48, 327-338.

Evans, J.P., Forster, C.B., Goddard, J.V., 1997. Permeability of fault-related rocks, and implications for hydraulic structure of fault zones. Journal of Structural Geology, 19, 1393-1404

Fellgett, M.W., Kingdon, A., Williams, J.D.O., Gent, C.M.A., 2017. State of stress across UK regions. British Geological Survey GeoAnalytics and Modelling Directorate Open Report OR/17/048, 60 pp. http://nora.nerc.ac.uk/id/eprint/517414/1/OR17048.pdf

Ford, T.D., Torrens, H.S., 2001. A Farey story: the pioneer geologist John Farey (1766–1826). Geology Today, 17 (2), 59-68.

Foulger, G.R., Wilson, M.P., Gluyas, J.G., Julian, B.R., Davies, R.J., 2018. Global review of human-induced earthquakes. Earth-Science Reviews, 178, 438–514.

Gallois, R.W., Worssam, B.C., 1993. The geology of the country around Horsham: memoir for 1:50,000 geological map sheet 302 (England and Wales). H.M.S.O., London, 130 pp.

Gans, C.R., Furlong, K.P., Malservisi, R., 2003. Fault creep and microseismicity on the Hayward fault, California: Implications for asperity size. Geophysical Research Letters, 30, 2000, 4 pp., doi: 10.1029/2003GL017904

GeoSierra, 2017. Review of 2011 Preese Hall Well Stimulations and Proposed Alternate Stimulation Method for UK Bowland-Hodder Shale Gas. GeoSierra LLC, Norcross, Georgia. http://www.geosierra.com/files/122554754.pdf

GeoSierra, 2019. Newdigate Seismicity and Link to Horse Hill HH-1 Well Activities. GeoSierra LLC, Norcross, Georgia. http://www.geosierra.com/files/132555955.pdf

Gilfillan, S., Haszeldine, S., McGuire, B., Selley, R., 2018. Surrey quake fears. Letter to the Editor, The Times, 6 August 2018.

Goebel, T.H.W., Weingarten, M., Chen, X., Haffener, J., Brodsky, E.E., 2017. The 2016 M_w 5.1 Fairview, Oklahoma earthquakes: Evidence for long-range poroelastic triggering at >40 km from fluid disposal wells. Earth and Planetary Science Letters, 472, 50–61.

Gölke, M., Coblentz, D., 1996. Origins of the European regional stress field. Tectonophysics, 266, 11-24.

Grasso, J.R., Wittlinger, G., 1990. Ten years of seismic monitoring over a gas field area. Bulletin of the Seismological Society of America, 80, 450-474.

Grigoli, F., Cesca, S., Rinaldi, A.P., Manconi, A., López-Comino, J.A., Clinton, J.F., Westaway, R., Cauzzi, C., Dahm, T., Wiemer, S., 2018. The November 2017 M_w 5.5 Pohang earthquake: A possible case of induced seismicity in South Korea. Science, 360, 1003-1006.

Grünthal, G., 1998. European Macroseismic Scale 1998, EMS-98. Cahiers du Centre Européen de Géodynamique et de Séismologie, 15. Centre Européen de Géodynamique et de Séismologie, Luxembourg, 101 pp.

Guo BoYun, Sun Kai, Ghalambor, A., eds., 2008. Well Productivity Handbook. Elsevier, London, 334 pp.

GVL, 2018. United Kingdom Relative Deformation Map. Geomatic Ventures Limited, Nottingham. https://mangomap.com/geomatic-ventures-limited/maps/72883/united-kingdom-relative-deformation-map?preview=true

Haines, T., Michie, E.A.H, Neilson, J.E., Healy, D., 2016. Permeability evolution across carbonate hosted normal fault zones. Marine and Petroleum Geology, 72, 62-82.

Hainzl, S., 2004. Seismicity patterns of earthquake swarms due to fluid intrusion and stress triggering. Geophysical Journal International, 159, 1090–1096.

Harbord, C.W.A., Nielsen, S.B., De Paola, N., Holdsworth, R.E., 2017. Earthquake nucleation on rough faults. Geology, 45, 931–934.

Harding, P., Bridgland, D.R., Allen, P., Bradley, P., Grant, M.J, Peat, D., Schwenninger, J.-L., Scott, R., Westaway, R., White, T.S., 2012 Chronology of the Lower and Middle Palaeolithic in NW Europe: developer-funded investigations at Dunbridge, Hampshire, southern England. Proceedings of the Geologists' Association, 123, 584-607.

Haszeldine, S., Cavanagh, A., 2018. Weald Basin 2018 Earthquake Cluster Analysis: Does Horse Hill meet Davis & Frohlich (1993) criteria for induced earthquakes? https://www.ogauthority.co.uk/media/5173/10-weald-basin-earthquakes-induced-oga-workshop-haszeldine-cavanagh-oct-2018-low-res.pdf

Hawkes, P.W., Fraser, A.J., Einchcomb, C.C.G., 1998. The tectono-stratigraphic development and tectonic history of the Weald and Wessex Basins, Southern England. In: Underhill, J.R. (ed.), The Development, Evolution and Petroleum Geology of the Wessex Basin. Geological Society, London, Special Publications, 133, 33-69.

Hayhurst, R., 2018. Oil company says "We're not to blame for Surrey earthquake" – but local concerns remain. Drill or Drop? Magazine. https://drillordrop.com/2018/04/04/oil-company-says-were-not-to-blame-for-surrey-earthquake-but-local-concerns-remain/

Hayhurst, R., 2019. Latest earth tremor prompts call for release of data on oil operations. Drill or Drop? Magazine. https://drillordrop.com/2019/05/10/latest-earth-tremor-prompts-call-for-release-of-data-on-oil-operations/

Heidbach, O., Rajabi, M., Cui, X., Fuchs, K., Müller, B., Reinecker, J., Reiter, K., Tingay, M., Wenzel, F., Xie, F., Ziegler, M.O., Zoback, M.-L., Zoback, M.D., 2018. The World Stress Map database release 2016: Crustal stress pattern across scales. Tectonophysics, 744, 484-498.

Hesselbo, S.P., Jenkyns, H.C.A., 1995. A comparison of the Hettangian to Bajocian successions of Dorset and Yorkshire. In Taylor, P.D. (Ed.), Field geology of the British Jurassic. Geological Society, London, pp. 105-150.

Hettema, M., Papamichos, E., Schutjens, P., 2002. Subsidence delay: Field observations and analysis. Oil & Gas Science and Technology, 57, 443–458.

Hicks, S., Verdon, J., Baptie, B., Luckett, R., Mildon, Z., Gernon, T., 2019. A shallow earthquake swarm close to hydrocarbon activities: discriminating between natural and induced causes for the 2018–19 Surrey, UK earthquake sequence, Seismological Research Letters, https://pubs.geoscienceworld.org/ssa/srl/article-pdf/doi/10.1785/0220190125/4819219/srl-2019125.1.pdf

Hincks, T., Aspinall, W., Cooke, R, Gernon, T., 2018. Oklahoma's induced seismicity strongly linked to wastewater injection depth. Science, 359, 1251-1255.

Hitzman, M.W., Clarke, D.D., Detournay, E., Dieterich, J.H., Dillon, D.K., Green, S.J., Habiger, R.M., McGuire, R.K., Mitchell, J.K., Shemeta, J.E., Smith, J.L., 2013. Induced Seismicity Potential in Energy Technologies. The National Academies Press, Washington, DC, 263 pp. http://www.nap.edu/catalog/13355/induced-seismicity-potential-inenergy-technologies.

Holland, A.A., 2013. Earthquakes triggered by hydraulic fracturing in south-central Oklahoma. Bulletin of the Seismological Society of America, 103, 1784-1792.

Hornbach, M.J., DeShon, H.R., Ellsworth, W.L., Stump, B.W., Hayward, C., Frohlich, C., Oldham, H.R., Olson, J.E., Magnani, M.B., Brokaw, C., Luetgert, J.H., 2015. Causal factors for seismicity near Azle, Texas. Nature Communications, 6, 7728, 11 pp., doi: 10.1038/ncomms7728

Hornbach, M.J., Jones, M., Scales, M., DeShon, H.R., Magnani, M.B., Frohlich, C., Stump, B., Hayward, C., Layton, M., 2016. Ellenburger wastewater injection and seismicity in North Texas. Physics of the Earth and Planetary Interiors, 261, 54–68.

Horse Hill Developments Ltd., 2018a. FACTS ABOUT HORSE HILL. What we ARE doing & what we ARE NOT doing. Horse Hill Developments Ltd., London.

http://www.horsehilldevelopments.co.uk/ul/FACTS%20about%20HH%20Final%20Draft%20181018.pdf

Horse Hill Developments Ltd., 2018b. Horse Hill-1 rig-less intervention and well testing programme. Report HHDL-HH1-RIWTP-R0. Horse Hill Developments Ltd., London, 81 pp. https://brockhamoilwell.files.wordpress.com/2019/04/disclosure-201808357-2.pdf

Howett, F., 1964. Stratigraphy and structure of the Purbeck inliers of Sussex (England). Quarterly Journal of the Geological Society, London, 120, 77-113.

Igonin, N., Verdon, J.P., Kendall, J-M., Eaton, D.W., 2019. The importance of pre-existing fracture networks for fault reactivation during hydraulic fracturing. Earth and Space Science Open Archive, 10500976, 27 pp., doi: 10.1002/essoar.10500976.1. https://www.essoar.org/doi/pdf/10.1002/essoar.10500976.1

Jacob, C.E., 1940. The flow of water in an elastic artesian aquifer. Transactions of the American Geophysical Union, 2, 574-586.

Jones, H K, Morris, B L, Cheney, C S, Brewerton, L J, Merrin, P D, Lewis, M A, MacDonald, A M, Coleby, L M, Talbot, J C, McKenzie, A A, Bird, M J, Cunningham, J, and Robinson, V K. 2000. The physical properties of minor aquifers in England and Wales. British Geological Survey Technical Report, WD/00/4, 234 pp. Environment Agency R&D Publication 68.

Justinic, A.H., Stump, B., Hayward, C., Frohlich, C., 2013. Analysis of the Cleburne, Texas earthquake sequence from June 2009 to June 2010. Bull. Seismol. Soc. Am., 103, 3083–3093.

Karner, G.D., Lake, S.D., Dewey, J.F., 1987. The thermal and mechanical development of the Wessex Basin, southern England. In: Coward, M.P., Dewey, J.F., Hancock, P.L. (eds), Continental Extensional Tectonics. Geological Society, London, Special Publications, 28, 517-536.

Keranen, K.M., Weingarten, M., Abers, G.A., Bekins, B.A., Ge SheMin, 2014. Sharp increase in central Oklahoma seismicity since 2008 induced by massive wastewater injection. Science, 345, 448–451.

Kim Won-Young, 2013. Induced seismicity associated with fluid injection into a deep well in Youngstown, Ohio. Journal of Geophysical Research Solid Earth, 118, 3506–3518.

Kingdon, A., Fellgett, M.W., Williams, J.D.O., 2016. Use of borehole imaging to improve understanding of the *in-situ* stress orientation of Central and Northern England and its implications for unconventional hydrocarbon resources. Marine and Petroleum Geology, 73, 1-20.

Klein, R.J., Barr, M.V., 1986. Regional state of stress in Western Europe. In: Stephansson, O. (Ed.), Proceedings of the International Symposium on Rock Stress and Rock Stress Measurements, Stockholm, 1-3 September 1986. Centek, Lulea, pp. 33-44.

Kovach, R.L., 1974. Source mechanisms for Wilmington oil field, California, subsidence earthquakes. Bulletin of the Seismological Society of America, 64, 699-711.

Lake, S.D., Karner, G.D., 1987. The structure and evolution of the Wessex Basin, southern England: an example of inversion tectonics. Tectonophysics, 137, 347-356, 358-378.

Lang, W.D., 1914. The geology of Charmouth cliffs, beach and fore-shore. Proceedings of the Geologists' Association, 25, 293-360.

Lang, W.D., Spath, L.F., Richardson, W.A., 1923. Shales-with-'Beef', a sequence in the Lower Lias of the Dorset coast. Quarterly Journal of the Geological Society, London, 79, 47-99.

Lash, G.G., Engelder, T., 2005. An analysis of horizontal microcracking during catagenesis: Example from the Catskill delta complex. AAPG Bulletin, 89, 1433-1449.

Lewis, M.A., Cheney, C.S., Ó Dochartaigh, B.É., 2006. Guide to Permeability Indices. British Geological Survey, Information Products Programme, Open Report CR/06/160N. British Geological Survey, Keyworth, Nottingham, 29 pp.

Lunn, R.J., Shipton, Z.K., Bright, A.M., 2008. How can we improve estimates of bulk fault zone hydraulic properties? In: Wibberley, C.A.J., Kurtz, W., Imber, J., Holdsworth, R.E., Collettini, C. (eds), The Internal Structure of Fault Zones: Implications for Mechanical and Fluid-Flow Properties. Geological Society, London, Special Publications, 299, 231–237.

Maher Jr, H.D., Ogata, K., Braathen, A., 2017. Cone-in-cone and beef mineralization associated with Triassic growth basin faulting and shallow shale diagenesis, Edgeøya, Svalbard. Geological Magazine, 154, 201–216.

McDermott, R.G., Ault, A.K., Evans, J.P., Reiners, P.W., 2017. Thermochronometric and textural evidence for seismicity via asperity flash heating on exhumed hematite fault mirrors, Wasatch fault zone, UT, USA. Earth and Planetary Science Letters, 471, 85-93.

McKenzie, D.P., 1969. The relationship between fault plane solutions for earthquakes and the directions of the principal stresses. Bulletin of the Seismological Society of America, 59, 591–601.

McLennan, W., 2019. Surrey earthquakes: Is oil drilling causing tremors? British Broadcasting Corporation, London. https://www.bbc.co.uk/news/uk-england-47816810

McLimans, R.K., Videtich. P.E., 1989. Diagenesis and burial history of Great Oolite Limestone, southern England. American Association of Petroleum Geologists Bulletin, 73, 1195-1205.

Meng QingFeng, Hooker, J., Cartwright, J., 2017. Early overpressuring in organic-rich shales during burial: evidence from fibrous calcite veins in the Lower Jurassic Shales-with-Beef Member in the Wessex Basin, UK. Journal of the Geological Society, London, 174, 869-882.

Meng QingFeng, Hooker, J., Cartwright, J., 2018. Displacive widening of calcite veins in shale: Insights into the force of crystallization. Journal of Sedimentary Research, 88, 327-343.

Mitchell, E.K., Fialko, Y., Brown, K.M., 2012. Temperature dependence of frictional healing of Westerly granite: experimental observations and numerical simulations. Geochemistry, Geophysics, Geosystems, 14, 567–582.

Newson, M.D., 1973. The Carboniferous Limestone of the UK as an aquifer rock. The Geographical Journal, 139 (2), 294-305.

OGA, 2018. OGA Newdigate Seismicity Workshop –3 October 2018. Summary and conclusion. UK Oil & Gas Authority, Aberdeen. https://www.ogauthority.co.uk/media/5174/2018_11_23-newdigate-workshop-summary-finalv3.pdf

OGA, 2019. Interim report of the scientific analysis of data gathered from Cuadrilla's operations at Preston New Road. UK Oil & Gas Authority, Aberdeen, 20 pp. https://www.ogauthority.co.uk/onshore/onshore-reports-and-data/preston-new-road-pnr-1z-hydraulic-fracturing-operations-data/

Ottemöller, L., Nielsen, H., Atakan, K., Braunmiller, J., Havskov, J., 2005. The 7 May 2001 induced seismic event in the Ekofisk oil field, North Sea. Journal of Geophysical Research, 110, B10301, 15 pp., doi: 10.1029/2004jb003374.

Parnell, J., Honghan, C., Middleton, D., Haggan, T., Carey, P., 2000. Significance of fibrous mineral veins in hydrocarbon migration: fluid inclusion studies. Journal of Geochemical Exploration, 69, 623-627.

Pennington, W.D., Davis, S.D., Carlson, S.M., Dupree, J., Ewing, T.E., 1986. The evolution of seismic barriers and asperities caused by the depressuring of fault planes in oil and gas fields of South Texas. Bulletin of the Seismological Society of America, 76, 939-948.

Pine, R.J., Batchelor, A.S., 1984. Downward migration of shearing in jointed rock during hydraulic injections. International Journal of Rock Mechanics and Mining Sciences & Geomechanics Abstracts 21, 249-263.

Pratt, W.E., Johnson, D.W., 1926. Local subsidence of the Goose Creek oil field. Journal of Geology, 34, 577–590.

Pruiksma, J.P., Rózsás, Á., 2017. Vibration levels at foundations of houses in Groningen due to induced earthquakes. Report 2017 R10493-A. TNO, Utrecht, The Netherlands, 115 pp.

Pullan, C.P., Butler, M., 2018. Paleozoic gas potential in the Weald Basin of southern England. In: Paleozoic Plays of NW Europe, Monaghan, A.A., Underhill, J.R., Hewett, A.J., Marshall, J.E.A. (eds). Geological Society, London, Special Publications, 471, 333-363.

Reiter, M., 1999. Stress analyses of a simple fault asperity. In: Vail Rocks 1999, The 37th U.S. Symposium on Rock Mechanics, 7-9 June 1999, Vail, Colorado. American Rock Mechanics Association paper ARMA-99-0391, 8 pp.

Rothé, G.H., Lui, C.Y., 1983. Possibility of induced seismicity in the vicinity of the sleepy hollow oil field, southwestern Nebraska. Bulletin of the Seismological Society of America, 73, 1357-1367.

Schultz, R., Stern, V., Novakovic, M., Atkinson, G., Gu, Y.J., 2015. Hydraulic fracturing and the Crooked Lake sequences: Insights gleaned from regional seismic networks. Geophysical Research Letters, 42, 2750-2758.

Segall, P., 1989. Earthquakes triggered by fluid extraction. Geology, 17, 942–946.

Segall, P., Fitzgerald, S.D., 1998. A note on induced stress changes in hydrocarbon and geothermal reservoirs. Tectonophysics, 289, 117–128.

Selvadurai, P.A., Glaser, S.D., 2017. Asperity generation and its relationship to seismicity on a planar fault: a laboratory simulation. Geophysical Journal International, 208, 1009–1025.

Shepley, M.G., 2007. Analysis of flows from a large Carboniferous Limestone drainage adit, Derbyshire, England. Quarterly Journal of Engineering Geology and Hydrology, 40, 123-135.

Simpson, D.W., Leith, W., 1985. The 1976 and 1984 Gazli, USSR, earthquakes were induced? Bulletin of the Seismological Society of America, 75, 1465-1468.

Simpson, D.W., Leith, W.S., Scholz, C.H., 1988. Two types of reservoir-induced seismicity. Bulletin of the Seismological Society of America, 78, 2025-2040.

Spetzler, J., Dost, B., 2017. Hypocentre estimation of induced earthquakes in Groningen. Geophysical Journal International, 209, 453–465.

Stoneley, R., 1982. The structural development of the Wessex Basin. Journal of the Geological Society, London, 139, 543-552.

Tarney, J., Schreiber, B.C., 1977. Cone-in-cone and beef-in-shale textures from DSDP Site 330, Falkland Plateau, South Atlantic. Deep Sea Drilling Project Initial Reports, 36, 865-870.

Townend, J., Zoback, M.D. 2000. How faulting keeps the crust strong. Geology, 28, 399–402.

Trueman, S., 2003. The Humbly Grove, Herriard, Storrington, Singleton, Stockbridge, Goodworth, Horndean, Palmers Wood, Bletchingley and Albury Fields, Hampshire, Surrey and Sussex, UK Onshore. In: Gluyas, J., Hitchens, H.M. (eds.), United Kingdom Oil and Gas Fields Commemorative Millennium Volume. Geological Society, London, Memoir 20, pp. 929-941.

UKOG, 2019a. Why earth tremors in Surrey should not be blamed on oil exploration. Statement from UK Oil & Gas Plc, in response to "unscientific" claims made by Dr Cavanagh, Dr Gilfillan and Professor Haszeldine. UK Oil & Gas Plc, London. https://www.ukogplc.com/ul/Technical%20Response%20to%20Edinburgh%20University%20120419.pdf

UKOG, 2019b. Horse Hill Overview. UK Oil & Gas Plc, London. https://www.ukogplc.com/page.php?pID=60

UKOG, 2019c. HH-1 and HH-2z extended well test update. UK Oil & Gas Plc, London, 23 December 2019. https://www.lse.co.uk/rns/UKOG/hh-1-and-hh-2z-extended-well-test-update-xjk6frv4uqebsr1.html

UKOG, 2020a. Horse Hill-2z water shut off intervention commences. UK Oil & Gas Plc, London, 19 February 2020. https://irpages2.equitystory.com/websites/rns_news/English/1100/news-tool---rns---eqs-group.html?article=30267363&company=ukog

UKOG, 2020b. Dry oil flows to surface following successful Horse Hill-2z water shut-off programme. UK Oil & Gas Plc, London. 9 March 2020. https://irpages2.equitystory.com/websites/rns_news/English/1100/news-tool---rns---eqs-group.html?article=30354960&company=ukog

Verdon, J.P., Baptie, B.J., Bommer, J.J., 2019. An improved framework for discriminating seismicity induced by industrial activities from natural earthquakes. Seismological Research Letters, 90, 1592-1611.

Wald, D.J., Quitoriano, V., Heaton, T.H., Kanamori, H. 1999. Relationships between peak ground acceleration, peak ground velocity, and modified Mercalli intensity in California. Earthquake Spectra, 15, 557–564.

Walsh, F.R., Zoback, M.D., 2015. Oklahoma's recent earthquakes and saltwater disposal. Science Advances, 1, e1500195, 9 pp., doi: 10.1126/sciadv.1500195.

Walsh, J.J., Watterson, J., 1988. Dips of normal faults in British Coal Measures and other sedimentary sequences. Journal of the Geological Society, London, 145, 859-873.

Wang QiQi, 2016. Characterization of bedding-parallel fractures in shale - Morphology, size distribution and spatial organization. Master of Science thesis, The University of Texas at Austin, 324 pp.

Webster, T., 1826. Observations on the Purbeck and Portland Beds. Transactions of the Geological Society, London, Series 2, 2, 37-44.

Wees, V.J., Buijze, L., van Thienen-Visser, K., Nepveu, M., Wassing, B., Orlic, B., Fokker, P., 2014. Geomechanics response and induced seismicity during gas field depletion in the Netherlands, Geothermics, 52, 206–219.

Weingarten, M., Ge SheMin, Godt, J.W., Bekins, B.A., Rubinstein, J.L., 2015. High-rate injection is associated with the increase in U.S. mid-continent seismicity. Science, 348, 1336–1340.

Weisstein, E.W., 2019. Erfc. From MathWorld - A Wolfram Web Resource. http://mathworld.wolfram.com/Erfc.html

Westaway, R., 2006. Investigation of coupling between surface processes and induced flow in the lower continental crust as a cause of intraplate seismicity. Earth Surface Processes and Landforms 31, 1480-1509.

Westaway, R., 2016. The importance of characterizing uncertainty in controversial geoscience applications: induced seismicity associated with hydraulic fracturing for shale gas in northwest England. Proceedings of the Geologists' Association, 127, 1–17.

Westaway, R., 2017. Integrating induced seismicity with rock mechanics: a conceptual model for the 2011 Preese Hall fracture development and induced seismicity. In: Rutter, E.H., Mecklenburgh, J., Taylor, K.G. (eds). Geomechanical and Petrophysical Properties of Mudrocks. Geological Society, London, Special Publications, 454, 327–359.

Westaway, R., Bridgland, D.R., White, M.J., 2006. The Quaternary uplift history of central southern England: evidence from the terraces of the Solent River system and nearby raised beaches, Quaternary Science Reviews, 25, 2212-2250.

Westaway, R., Burnside, N.M., 2019. Fault 'corrosion' by fluid injection: potential cause of the November 2017 MW 5.5 Korean earthquake. Geofluids, 1280721, 23 pp., doi: 10.1155/2019/1280721

Westaway, R., Younger, P.L., 2014. Quantification of potential macroseismic effects of the induced seismicity that might result from hydraulic fracturing for shale gas exploitation in the UK. Quarterly Journal of Engineering Geology and Hydrogeology, 47, 333–350.

Westaway, R., Younger, P.L., 2016. Unravelling the relative contributions of climate change and ground disturbance to subsurface temperature perturbations: case studies from Tyneside, UK. Geothermics, 64, 490–515.

Westwood, R.F., Toon, S.M., Styles, P., Cassidy, N.J., 2017. Horizontal respect distance for hydraulic fracturing in the vicinity of existing faults in deep geological reservoirs: a review and modelling study. Geomechanics and Geophysics for Geo-Energy and Geo-Resources, 3, 379–391.

Wetmiller, R.J., 1986. Earthquakes near Rocky Mountain House, Alberta, and their relationship to gas production facilities. Canadian J. Earth Science, 23, 172-181.

Wigley, P., 2015. Exploration in the UK Weald Basin: Déjà vu. Search and Discovery, 70182, 8 pp. http://www.searchanddiscovery.com/pdfz/documents/2015/70182wigley/ndx_wigley.pdf.html

Willacy, C., van Dedem, E., Minisini, S., Li JunLun, Blokland, J.-W., Das, I., Droujinine, A., 2019. Full-waveform event location and moment tensor inversion for induced seismicity. Geophysics, 84 (2), KS39–KS57. doi: 10.1190/GEO2018-0212.1

Wilson, M.P., Worrall, F., Davies, R.J., Almond, S., 2018. Fracking: How far from faults? Geomechanics and Geophysics for Geo-Energy and Geo-Resources, 4, 193–199.

Worden, C.B., Gerstenberger, M.C., Rhoades, D.A., Wald, D.J., 2012. Probabilistic relationships between ground-motion parameters and modified Mercalli intensity in California. Bulletin of the Seismological Society of America, 102, 204-221.

Xodus, 2018. 2018 Competent Person's Report to UK Oil & Gas Investments PLC. Xodus Group, London, 112 pp. https://www.ukogplc.com/ul/UKOG%202018%20CPR%20060618.pdf

Yerkes, R.F., Castle, R.D., 1976. Seismicity and faulting attributed to fluid extraction. Engineering Geology, 10, 151-167.

Younger, P.L., 1993. Simple generalized methods for estimating aquifer storage parameters. Quarterly Journal of Engineering Geology, 26, 127-135.

Zanella, A., Cobbold, P.R., Boassen, T., 2015. Natural hydraulic fractures in the Wessex Basin, SW England: widespread distribution, composition and history. Marine and Petroleum Geology, 68, 438-448.

Zhang Bo, Yin CongYuan, Gu ZhiDong, Zhang JinJiang, Yan ShuYu, Wang Yang, 2015. New indicators from bedding-parallel beef veins for the fault valve mechanism. Science China: Earth Sciences, 58, 1320–1336.

Zhang, YiPeng, Person, M., Rupp, J., Ellett, K., Celia, M.A., Gable, C.W., Bowen, B., Evans, J., Bandilla, K., Mozley, P., Dewers, T., Elliot, T., 2013. Hydrogeologic controls on induced seismicity in crystalline basement rocks due to fluid injection into basal reservoirs. Groundwater, 51, 525–538.

Zimmerman, R.W., Bodvarsson, G.S., 1996. Hydraulic conductivity of rock fractures. Transport in Porous Media, 23, 1–30.

Zoback, M.L., Zoback, M.D., 2007. Lithosphere stress and deformation. Treatise on Geophysics, 6, 253-273.

Table 1: Stratigraphy of the Horse Hill 1 borehole

Table 2: Layered Velocity Model used by Hicks et al. (2019)

Table 3: Source parameters for Newdigate earthquakes with focal mechanisms

Table 4: Newdigate seismicity since the start of June 2019

Figure captions

Figure 1. Map of the study area, modified from Fig. 2(a) of Hicks et al. (2019). The original geographical (latitude-longitude) co-ordinate system has been retained, but 'greyed out', with a new co-ordinate system added, indexed to the British National Grid (BNG). As is discussed in the main text, the original scale bar by Hicks et al. (2019) is much too small and has also been 'greyed out'. Faults are identified thus: BHF, Box Hill Fault; BRF, Brockham Fault; BUF, Buckland Fault; CF, Crawley Fault; COF, Collendean Fault; FGF, 'Faygate Fault'; HF, Holmbush Fault; HHF, Horse Hill Fault; HWF, Holmwood Fault; KFF, Kingsfold Fault; LHF, Leigh Fault; NGF, Newdigate Fault; OKF, Ockley Fault; WB1F, Whiteberry-1 Fault; and WCF, Westcott Fault. Most of these structures are depicted as shown by Hicks et al. (2019), although some are misplaced, as discussed in the text. The Crawley and Holmwood faults, not recognized by Hicks et al. (2019), are shown schematically where they cross seismic line TWLD-90-15, the southward continuation of which (beyond the excerpt shown in Fig. 2) is also shown schematically. The 'Faygate Fault' is a mistaken concept by Hicks et al. (2019), so is shown 'greyed out' (see text and online supplement). Focal mechanisms are illustrated as standard equal area projections of the lower focal hemisphere, with compressional quadrants of the P-wave radiation pattern shaded. Horse Hill 1 well track is from https://ukogl.org.uk/map/php/well_deviation_survey.php?wellId=3041. The source of information for positions of seismic lines, including line TWLD-90-15, was not reported by Hicks et al. (2019); they are from the schematic location map provided by the UK Onshore Geophysical Library (https://ukogl.org.uk/), which is indexed to the BNG, and was transformed to geographical co-ordinates by Hicks et al. (2019). Seismograph station GATW ceased operation on 17 May 2019 due to

equipment theft. It was replaced by station GAT2, ~230 m northwest, which became operational from 6 June.

Figure 2. 2-D seismic section along seismic line TWLD-90-15, modified from Fig. 6 of Hicks et al. (2019). The original was indexed by Hicks et al (2019) to the British National Grid (BNG), rather than the geographical co-ordinates used for Fig. 1; as discussed in the online supplement, after careful consideration these co-ordinates were accepted as accurate. The labelled horizons were not explained by Hicks et al. (2019), but appear to be the top Portland Group, top Kimmeridge Clay Formation, and top Coralline Oolite Formation (cf. Table 4). Faults designated by Hicks et al. (2019) are identified thus: COF, Collendean Fault; LHF, Leigh Fault; and NGF, Newdigate Fault. CF denotes the Crawley Fault. Hicks et al. (2019) did not explain how they depth-converted this seismic section. As is discussed in the main text and online supplement, it is suspected that they used their velocity model for earthquake location (Table 2) for this depth conversion. Their depth scale is 'greyed out', whereas the new version, using the seismic interval velocities from the HH1 well (Table 1) is emphasized. Additional interpretation has also been added, including the interpreted top Penarth Group / base Lias Group reflector and its offset by the main strand of the Newdigate Fault, and some of the additional lesser fault strands forming the multi-stranded Newdigate fault zones, other strands being evident in Fig. 3 and in the uninterpreted version of this seismic section provided by Hicks et al. (2019) in their online supplement.

Figure 3. Excerpt from the record section for seismic line TWLD-90-15, as provided by UKOGL, illustrating the Newdigate Fault. As geo-located in the online supplement, this excerpt extends between BNG references TQ 21585 39125 and TQ 20326 46935, a distance of ~8 km.

Figure 4. Time series of Newdigate earthquakes and other activities affecting the Horse Hill 1 and Brockham X2 wells, based on Fig. 3 of Hicks et al. (2019). Note that their original Fig. 6(d) has been omitted as it depicts an incorrect timeline for production at Brockham up to 2016: the correct timeline is shown in Fig. 11 of Angus (2018). **(a)** Installation dates of stations forming the local temporary seismic monitoring network. From Fig. 3(a) of Hicks et al. (2019). **(b)** Detected earthquakes, cumulative number of events, and inferred variations in the completeness threshold magnitude M_C. From Fig. 3(b) of Hicks et al. (2019). Note that some of the magnitudes M_L depicted here differ slightly from those listed in Supplementary Fig. S2 of Hicks et al. (2019), which feature in discussion in the text. **(c)** Summary timeline for activities at the Horse Hill 1 well, indicating (based on the information sources discussed in the text and details in part (d)) the phases of production from each reservoir. Notes refer to details discussed in the text, thus, regarding the HH1 well: 1, first known intervention affecting the well, 5 April 2018; 2, removal of bridge plug that had isolated the Portland reservoir from the surface, 4 July 2018; 3, production from KL3; 4, production from KL4; and 5, 'co-mingled' production from both KL3 and KL4. Regarding the BRX2Y well, based on the timeline reported by Hicks et al. (2019): 6 denotes the restart of production on 22 March 2018; 7 denotes a later resumption, with injection of water starting on 25 June and (net) production restarting on 28 June (but with both injection and production occurring on 27 June); and 8 denotes the end of production on 15 October 2018. **(d)** More detailed operations timeline for activities at the Horse Hill 1 well, with flow-period averaged production and cumulative production over time. From Fig. 3(c) of Hicks et al. (2019), with further details, including dates, provided in their supplementary Table S4. The information provided by Hicks et al. (2019) is much more detailed than that which has been otherwise released into the public domain, and must have been obtained from the developer. However, their reporting of the information does not identify the hydrocarbon reservoirs to which the activities relate (see part (c)), which is essential to reveal the pattern of correlation between seismicity and activities affecting the Portland reservoir (see also the online supplement).

Figure 5. Cartoons summarizing the proposed conceptual model linking the Newdigate seismicity to reductions in fluid pressure in oil wells. **(a)** Large-scale processes. Production of oil (1) will reduce the pressure within the Portland reservoir near the production well. This will cause flow of oil towards the well from more distal parts of the reservoir (2). This will be accompanied by flow of groundwater into the volume vacated by the oil, which is inferred to be hydraulically connected to the 'hyper-permeable' fabric in the underlying Lower Portland Sandstone (3), which will cause flow within this fabric (4). This flow will draw groundwater from greater depths (5), up one or more strands of the Newdigate fault zone, which is assumed permeable, reducing the pressure in the section where this fault transects the Dinantian limestone. This pressure reduction will act to draw groundwater from the permeable Dinantian limestone into the fault (6). The associated compaction of the Dinantian limestone will cause separation of its two surfaces across the seismogenic fault (7). Surface interventions affecting the wells, such as bleeding pressure following shut-in, will reduce the pressure inside the well and have a similar overall effect. **(b)** Processes on a micro-structural scale on the seismogenic fault, where separation of the fault surfaces by a small distance Δx, from configuration (i) to configuration (ii), affects three model asperities (1, 2 and 3). After this change, at asperity 1 the fault surfaces are no longer in contact, at asperity 2 what was an interference fit between the fault surfaces has become a clearance fit, and at asperity 3 the rocks forming asperity 3 have decompressed elastically, so they remain in contact but with a reduced normal stress and thus a reduced limiting shear stress that can maintain fault stability.

Figure 6. Map of the structure of British National Grid 100 km × 100 km quadrangle TQ, showing the depth of base Jurassic (in feet below O.D., with contours at 200 ft intervals) and locations where the base Jurassic is offset by faults. H and N appear to denote the Holmwood, and Newdigate faults (cf. Figs 1 and 2), although the latter is misplaced. Modified from part of Fig. 4(a) of Butler and Pullan (1990).

Figure 7. Graphs of the predicted variation in pressure δP with distance x from the model seismogenic fault, calculated using equation (1) at times t of 1 week, 1 month and 1 year after a pressure change ΔP_O=-10 kPa is imposed in the fault. **(a)** For hydraulic diffusivity D=1 $m^2 s^{-1}$, representing Carboniferous Limestone. **(b)** For D=0.002 $m^2 s^{-1}$, representing crystalline basement rocks (after Zhang et al., 2013).

Figure 8. Mohr circle diagrams representing the state of stress at 2400 m depth associated with the Newdigate seismicity. **(a)** For a model stress field with σ_H=63.300 MPa, σ_V=54.300 MPa, and σ_h=39.200 MPa. Hydrostatic groundwater pressure P_f=23.544 MPa causes σ_H'=39.756 MPa, σ_V'=30.756 MPa, and σ_h'=15.656 MPa, resulting in σ_L'=28.723 MPa and σ_M'=27.706 MPa. The resolved shear stress and normal stress on the fault, 10.401 and 21.622 MPa, plot below the Coulomb failure line for c=0.6, indicating that the fault is stable. **(b)** For revised conditions consistent with the set of processes in Fig. 5, representing the average model stress field on the fault, given the reduced proportion of asperities that remain in frictional contact. Groundwater pressure adjusts by 0.010 MPa below its hydrostatic value, to P_f=23.534 MPa, and the principal stresses adjust to σ_H=65.130 MPa and σ_h=36.870 MPa keeping σ_V=54.300 MPa. As a result, σ_H'=41.956 MPa, σ_V'=30.766 MPa, and σ_h'=13.336 MPa, resulting in σ_L'=28.566 MPa and σ_M'=27.466 MPa. The resolved shear stress and normal stress on the fault, 12.199 and 20.332 MPa, now plot on the Coulomb failure line for c=0.6, indicating that the fault is frictionally unstable.

Table 1: Stratigraphy of the Horse Hill 1 borehole

Subdivision	MD (m)	TVDSS (m)	TWT (s)	V_I (m s^{-1})	Notes
Younger subdivisions (Early Cretaceous; Berriasian to Barremian)					
Weald Clay	7.6	-66.9	NR	ND	
Hastings Beds	158.5	84.0	NR	ND	
Grinstead Clay	211.8	137.3	NR	ND	
Lower Tunbridge Wells Sands	234.7	160.2	NR	ND	
Wadhurst Clay	245.4	170.8	NR	ND	
Ashdown Beds	298.1	223.6	NR	ND	
Purbeck Group (latest Jurassic and earliest Cretaceous; Tithonian and Berriasian)					
Purbeck Durlston Beds	396.8	322.3	NR	ND	1
Purbeck Carbonates	464.8	390.3	NR	ND	
Purbeck Main Anhydrite	604.7	530.2	0.370	2500	
Portland Group (Late Jurassic; Tithonian)					
Upper Portland Sandstone	622.4	547.7	0.384	2531	
Lower Portland Sandstone	708.4	632.5	0.451	5011	
Ancholme Group (latest Middle Jurassic and Late Jurassic; Callovian to Tithonian)					
Kimmeridge Clay	755.9	677.6	0.469	2787	
Kimmeridgian Micrite 1	851.3	765.4	0.532	2861	
Kimmeridgian Micrite 2	939.7	835.5	0.581	2961	
Top Corallian	1359.1	1139.0	0.786	3289	
Corallian Limestone	1523.7	1272.2	0.867	3743	
Oxford Clay	1539.2	1285.3	0.874	3540	
Kellaways Beds	1666.0	1403.9	0.941	3725	
Great Oolite Group (Middle Jurassic; Bathonian and Callovian)					
Cornbrash	1681.6	1418.8	0.949	2600	2
Main Great Oolite	1682.8	1420.1	0.950	5095	
Fuller's Earth	1732.8	1468.5	0.969	4886	
Inferior Oolite Group (Middle Jurassic; Aalenian and Bajocian)					
Inferior Oolite	1767.5	1502.7	0.983	5584	
Lias Group (Early Jurassic; Hettangian to Toarcian)					
Upper Lias	1941.6	1675.8	1.045	4244	
Middle Lias	2048.0	1781.9	1.095	4796	
Lower Lias	2158.3	1892.2	1.141	4301	
Older subdivisions (Triassic and older)					
Rhaetic	2470.1	2204.0	1.286	5318	
Mercia Mudstone	2528.6	2262.5	1.308	4434	3
Dolomitic Conglomerate	2581.7	2315.6	NR	ND	
Carboniferous Limestone	2593.2	2326.8	1.337	ND	
Upper Devonian	2659.4	2393.3	NR	ND	4
TD	2686.8	2420.7	NR	ND	5

Data for tops of stratigraphic subdivisions (as used by UKOGL; not all expressed using modern formal stratigraphic nomenclature, which is available from https://www.bgs.ac.uk/lexicon) are from the online well log (https://ukogl.org.uk/map/php/pdf.php?subfolder=wells\tops&filename=3041.pdf), supplemented by values from Pullan and Butler (2018), NR indicating 'not reported'. Measured Depth (MD) is measured below a datum at 66.9 m O.D., below the local ground level of 74.5 m O.D. at the wellhead, at TQ 25254 43600. TVDSS is True Vertical Depth below O.D.; TWT is echo time. Values of interval velocity, V_I, are determined in this study, ND indicating 'not determined'. Notes:

1., The Durlston Beds (or Durlston Formation) are nowadays regarded as earliest Cretaceous; the rest of the Purbeck Group is Late Jurassic.

2., The Cornbrash Formation is too thin here for its interval velocity to be reliably determined.

3., Interval velocity for the Mercia Mudstone and the Dolomitic Conglomerate combined

4., TVDSS for the top Devonian estimated given the vertical orientation of the deepest part of the well.

5., The well bottoms (at TD) in Upper Devonian mudstone.

Table 2. Velocity Model from Hicks et al. (2019)

H (km)	V_P (km s^{-1})	V_S (km s^{-1})
0.0	2.2	1.2
0.2	2.4	1.4
0.4	2.6	1.5
0.7	2.7	1.5
1.2	3.1	1.8
1.5	3.6	2.0
1.8	4.7	2.7
2.1	5.0	2.8
2.4	5.5	3.1
7.6	6.4	3.7
18.9	7.0	4.1
34.2	8.0	4.6

This velocity model was used by Hicks et al. (2019) for earthquake relocation and moment tensor inversion. H denotes the depth to the top of each layer; V_P and V_S denote the P-wave and S-wave velocities. Note that this velocity model is significantly slower that that in Table $1; it results in a two-way time to depth 2326.8 m, corresponding to the top of the Carboniferous Limestone at Horse Hill, of 1.466 s rather than the actual 1.337 s.

2326.8 m 1.337 1.4656

Table 3: Source parameters for Newdigate earthquakes with focal mechanisms

No.	Date	Time (UTC)	Epicentre (BNG reference)	Depth (m)	ΔN (m)	ΔE (m)	Δz (m)	$\Delta\alpha$ (°)	N_P	N_S	Δt_o (s)	z_{DD} (m)	M_L	M_W 1	M_W 2	z_C (m)	Strike (°)	Dip (°)	Rake (°)	f_C (Hz)	r_o (m)	$\Delta\sigma$ (MPa)
1	18 Jul 2018	03:59:56	TQ 22005 41393	1990	1397	803	1011	151	15	13	0.04	ND	2.01	2.20	2.03	2.00	282	74	178	6.4	48	0.25
2	18 Jul 2018	13:33:18	TQ 21920 41474	1860	1463	737	1014	145	15	15	0.02	ND	2.54	2.56	2.45	2.20	276	75	169	4.3	25	0.27
3	14 Feb 2019	07:43:33	TQ 22959 41543	2220	297	330	379	98	9	7	0.09	2050	2.47	2.52	2.27	2.80	255	86	173	7.7	142	1.05
4	19 Feb 2019	17:03:57	TQ 22872 41538	2050	220	429	393	106	5	4	0.04	2040	1.98	1.95	1.77	2.20	256	61	-163	11.2	86	0.56
5	27 Feb 2019	03:42:21	TQ 22622 41517	2110	286	352	316	98	14	11	0.13	2300	3.18	3.25	2.87	3.60	260	78	178	5.8	169	2.62
6	04 May 2019	00:19:19	TQ 22796 41516	2190	143	165	294	94	13	10	0.11	2440	2.35	2.31	2.17	2.40	255	85	167	16.9	64	8.06

Data from supplementary table S2 of Hicks et al. (2019). The events are numbered to match Fig. 1. For events 1 and 2 only conventional hypocentral locations were determined, which yielded the epicentral co-ordinates and focal depths. Double difference focal depths (z_{DD}) were not determined (ND). For the other events, the epicentral co-ordinates and z_{DD} are determined from the double difference location procedure and the 'Depth' by conventional location. ΔN, ΔE and Δz are the uncertainties in northing, easting, and depth, based for events 3-6 on the double difference solutions. $\Delta\alpha$ is the maximum gap between ray path azimuths to seismograph stations that recorded each event, N_P and N_S being the numbers of P- and S-wave records. Δt_o is the rms residual in origin time. M_L and M_W are local magnitude and moment magnitude. M_W 1 and the centroid depth z_C are determined from the moment tensor; M_W 2 is from P-wave spectra. Strike, Dip and Rake are for the nodal plane of the focal mechanism that is regarded as the fault plane, being subparallel to the Cudworth Fault (Fig. 2). Mean corner frequency f_C, source radius r_O, and stress drop $\Delta\sigma$ are determined from seismogram spectra.

Table 4: Newdigate seismicity since the start of June 2019

Date	Time (UTC)	Latitude (°N)	Longitude (°W)	BNG	Depth (km)	M_L	Note
9 June 2019	02:43:18.2	51.159	0.237	TQ 23382 41449	2.7	-0.5	
9 June 2019	23:00:15.0	51.133	0.295	TQ 19393 38462	3.3	-0.1	
6 July 2019	01:03:20.4	51.161	0.242	TQ 23027 41663	2.5	-0.7	
6 July 2019	01:03:23.7	51.161	0.242	TQ 23027 41663	2.5	-0.7	
6 July 2019	01:03:30.1	51.159	0.241	TQ 23102 41442	2.1	-0.8	
6 July 2019	01:03:40.2	51.159	0.241	TQ 23102 41442	2.2	-0.7	
6 July 2019	03:57:15.3	51.160	0.239	TQ 23239 41557	2.5	0.1	
20 July 2019	22:02:26.0	51.158	0.251	TQ 22405 41315	2.1	-0.6	
29 July 2019	03:35:25.5	51.160	0.242	TQ 23029 41552	2.2	-0.1	
6 Aug 2019	02:32:00.9	51.157	0.239	TQ 23247 41223	2.2	-0.5	
12 Aug 2019	00:46:46.6	51.160	0.241	TQ 23099 41554	2.1	-0.7	
12 Aug 2019	00:46:49.2	51.160	0.241	TQ 23099 41554	2.1	-1.4	
2 Sep 2019	05:13:04.9	51.160	0.237	TQ 23379 41560	2.0	1.1	1
3 Sep 2019	20:19:13.2	51.161	0.237	TQ 23376 41672	2.0	0.2	
6 Sep 2019	07:09:45.5	51.161	0.237	TQ 23376 41672	2.0	1.0	
21 Sep 2019	14:43:45.2	51.160	0.237	TQ 23379 41560	2.2	0.6	
31 Oct 2019	19:25:16.4	51.160	0.238	TQ 23309 41558	2.0	0.8	

Cataloguing here is complete to 27 April 2020. Data are from https://earthquakes.bgs.ac.uk; these earthquakes have been located using standard BGS procedures, as reported by the International Seismological Centre (http://www.isc.ac.uk). Co-ordinate transformations to the British National Grid, as part of this study, use https://www.bgs.ac.uk/data/webservices/convertForm.cfm

Note:

1…Felt in Newdigate; maximum EMS intensity 2.

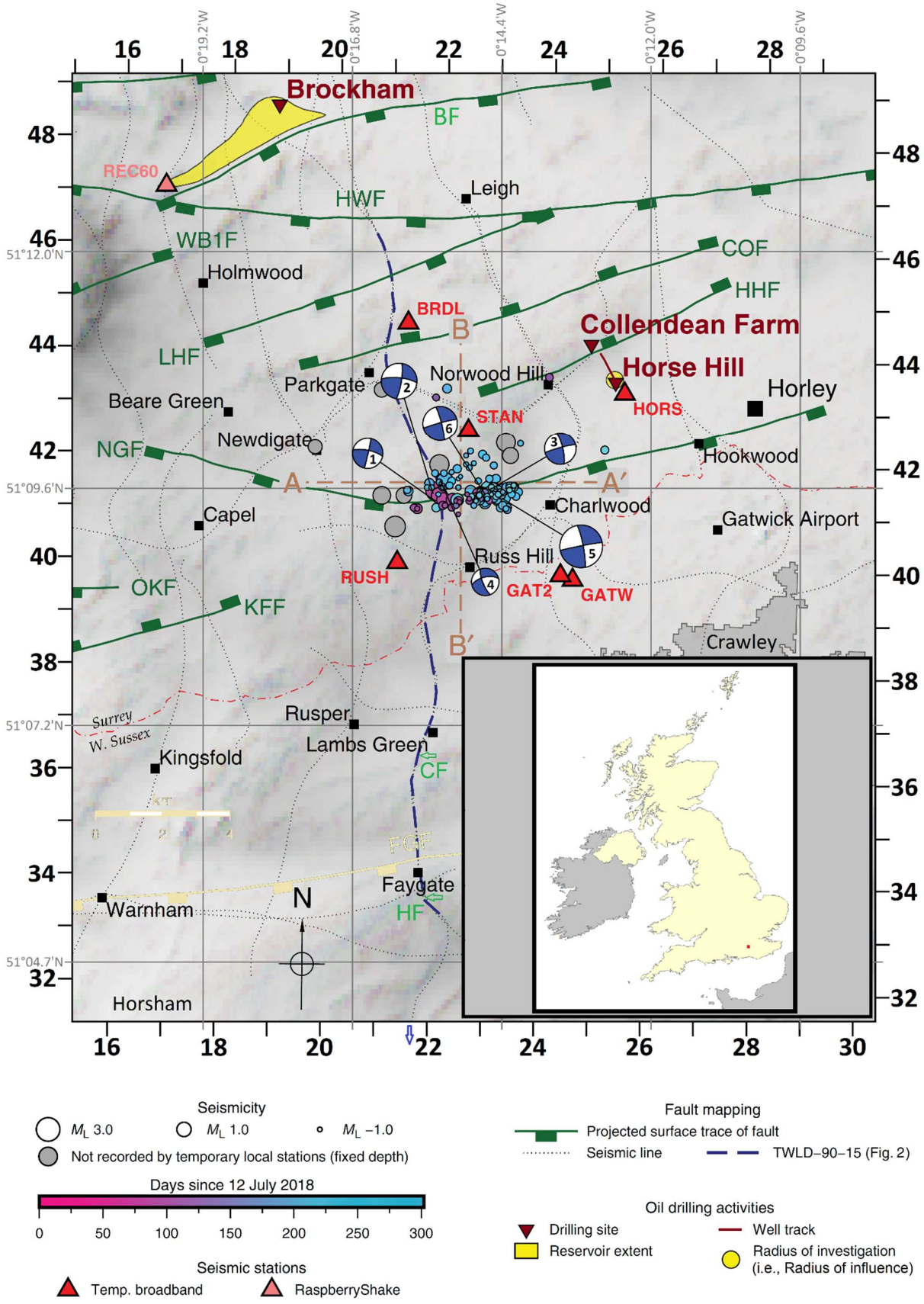
Brockham
REC60
BF
HWF
WB1F
COF
HHF
LHF
NGF
OKF
KFF
Leigh
Holmwood
BRDL
Collendean Farm
Horse Hill
HORS
Parkgate
Norwood Hill
Horley
Beare Green
STAN
Newdigate
Hookwood
Charlwood
Gatwick Airport
Capel
Russ Hill
RUSH
GAT2
GATW
Crawley
Rusper
Lambs Green
CF
Kingsfold
Surrey
W. Sussex
FGF
Faygate
HF
Warnham
Horsham
N
A
A′
B
B′
16
18
20
22
24
26
28
30
32
34
36
38
40
42
44
46
48
0°19.2'W
0°16.8'W
0°14.4'W
0°12.0'W
0°09.6'W
51°12.0'N
51°09.6'N
51°07.2'N
51°04.7'N
Seismicity
M_L 3.0
M_L 1.0
M_L −1.0
Not recorded by temporary local stations (fixed depth)
Days since 12 July 2018
0
50
100
150
200
250
300
Seismic stations
Temp. broadband
RaspberryShake
Fault mapping
Projected surface trace of fault
Seismic line
TWLD–90–15 (Fig. 2)
Oil drilling activities
Drilling site
Reservoir extent
Well track
Radius of investigation
(i.e., Radius of influence)

Figure 1

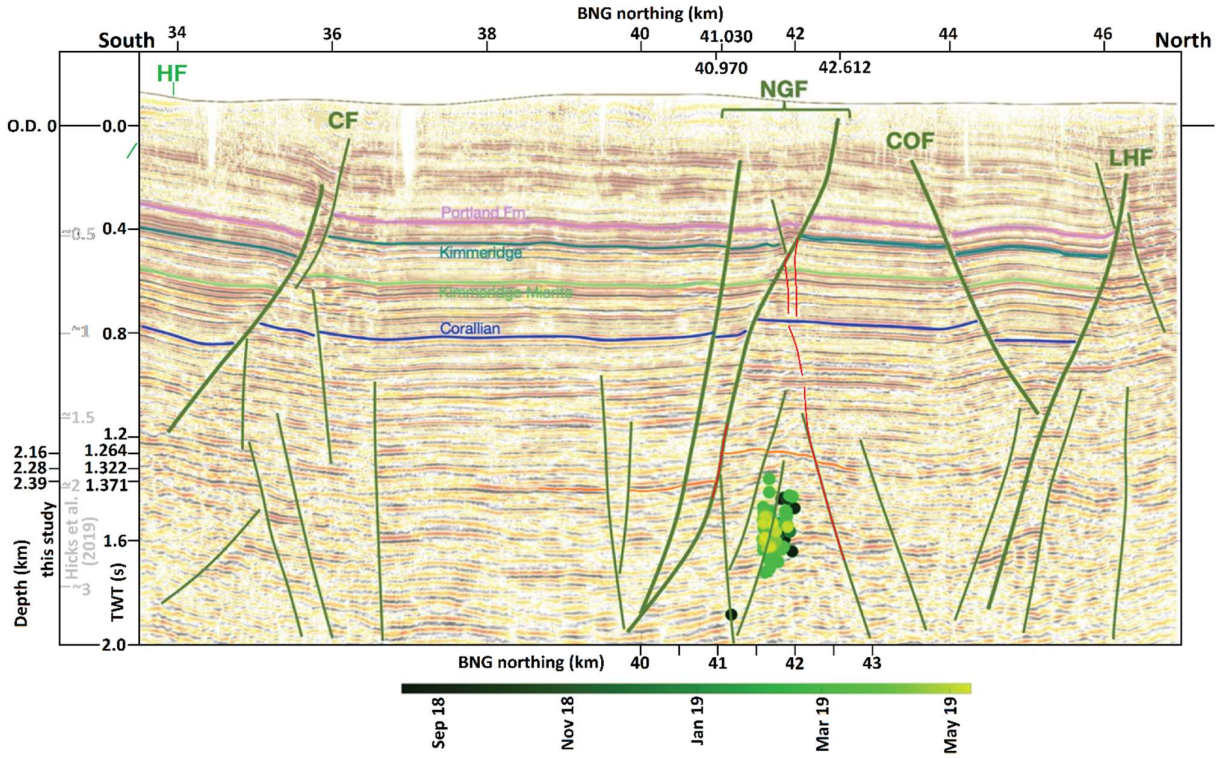
BNG northing (km)
South
North
34
36
38
40
41.030
42
44
46
40.970
42.612
HF
CF
NGF
COF
LHF
Portland Fm.
Kimmeridge
Kimmeridge Mbr 1a
Corallian
O.D. 0
0.0
0.4
0.8
1.2
1.264
1.322
1.371
1.6
2.0
2.16
2.28
2.39
Depth (km)
this study
Hicks et al. (2019)
TWT (s)
BNG northing (km)
40
41
42
43
Sep 18
Nov 18
Jan 19
Mar 19
May 19

Figure 2

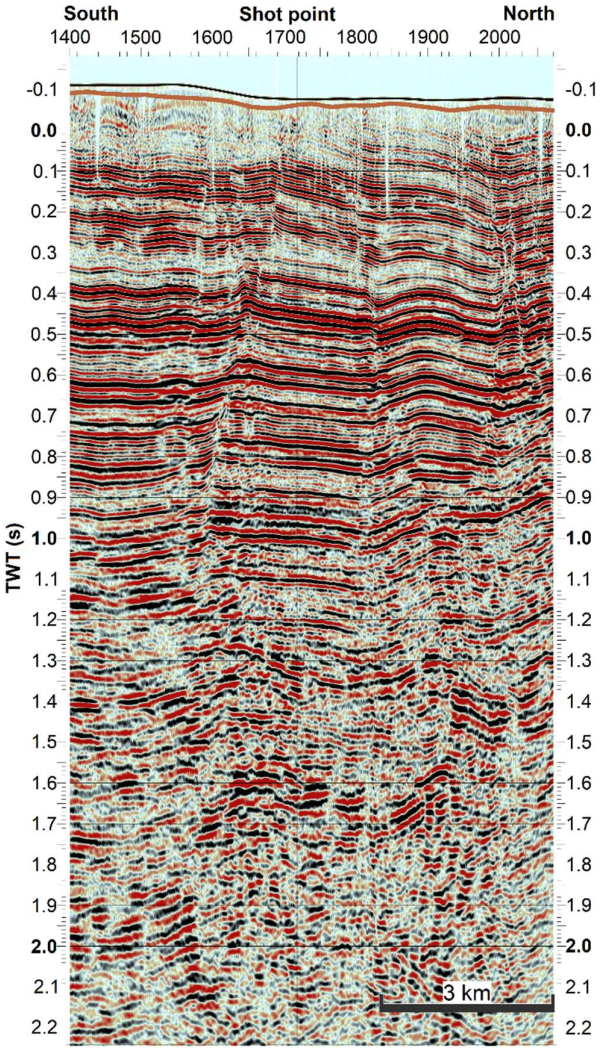
South
Shot point
North
1400
1500
1600
1700
1800
1900
2000
TWT (s)
-0.1
0.0
0.1
0.2
0.3
0.4
0.5
0.6
0.7
0.8
0.9
1.0
1.1
1.2
1.3
1.4
1.5
1.6
1.7
1.8
1.9
2.0
2.1
2.2
3 km

Figure 3

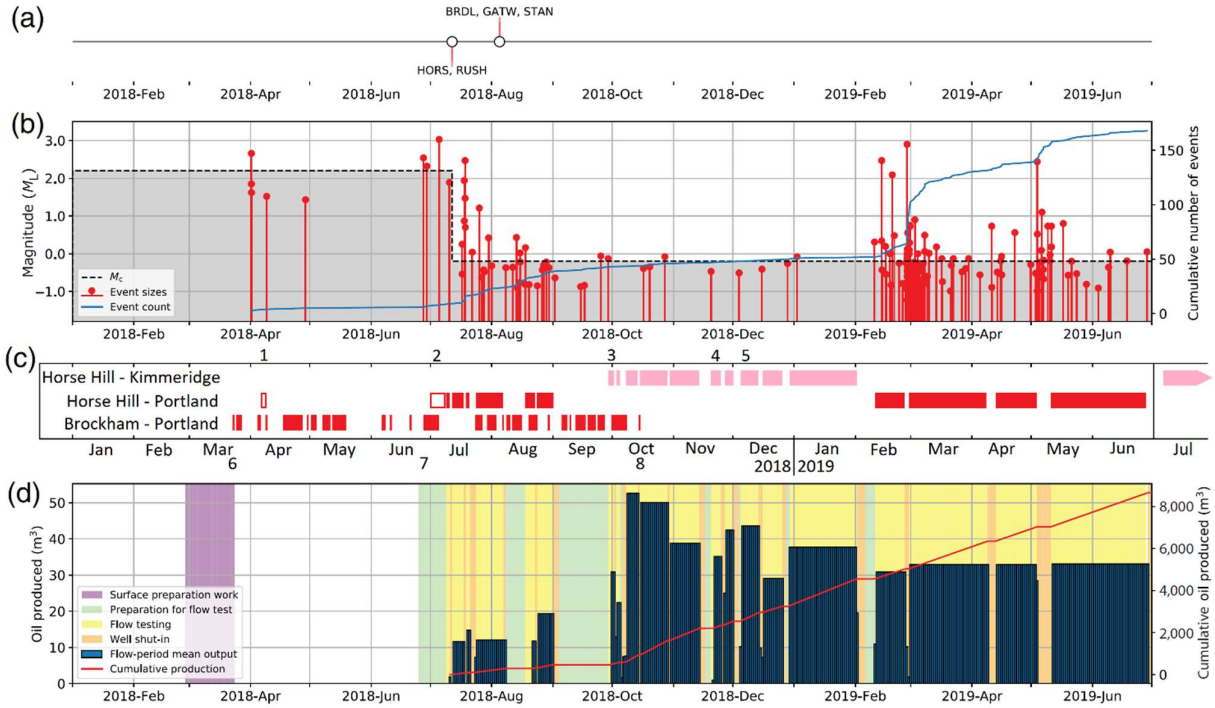
(a)
BRDL, GATW, STAN
HORS, RUSH
2018-Feb
2018-Apr
2018-Jun
2018-Aug
2018-Oct
2018-Dec
2019-Feb
2019-Apr
2019-Jun
(b)
Magnitude (M_L)
Cumulative number of events
M_c
Event sizes
Event count
1
2
3
4
5
(c)
Horse Hill - Kimmeridge
Horse Hill - Portland
Brockham - Portland
Jan
Feb
Mar
Apr
May
Jun
Jul
Aug
Sep
Oct
Nov
Dec
2018
2019
6
7
8
(d)
Oil produced (m³)
Cumulative oil produced (m³)
Surface preparation work
Preparation for flow test
Flow testing
Well shut-in
Flow-period mean output
Cumulative production

Figure 4

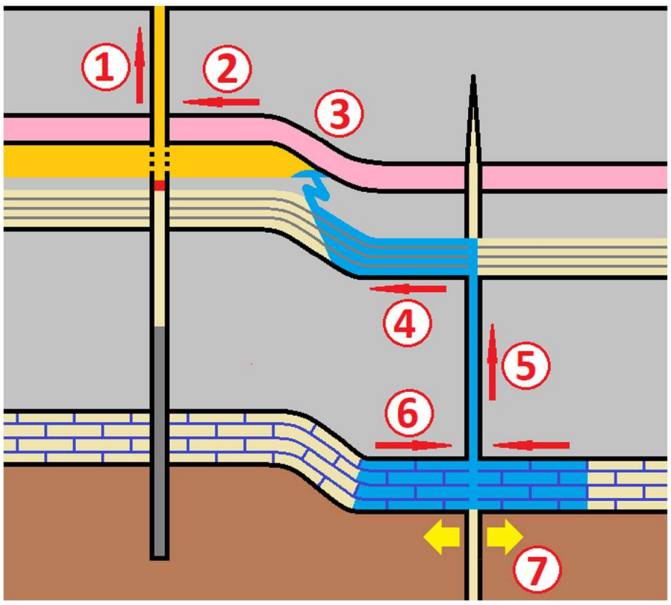

(a)

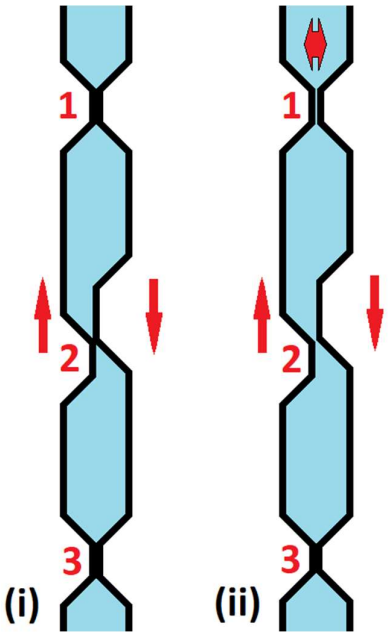

(b)

Figure 5

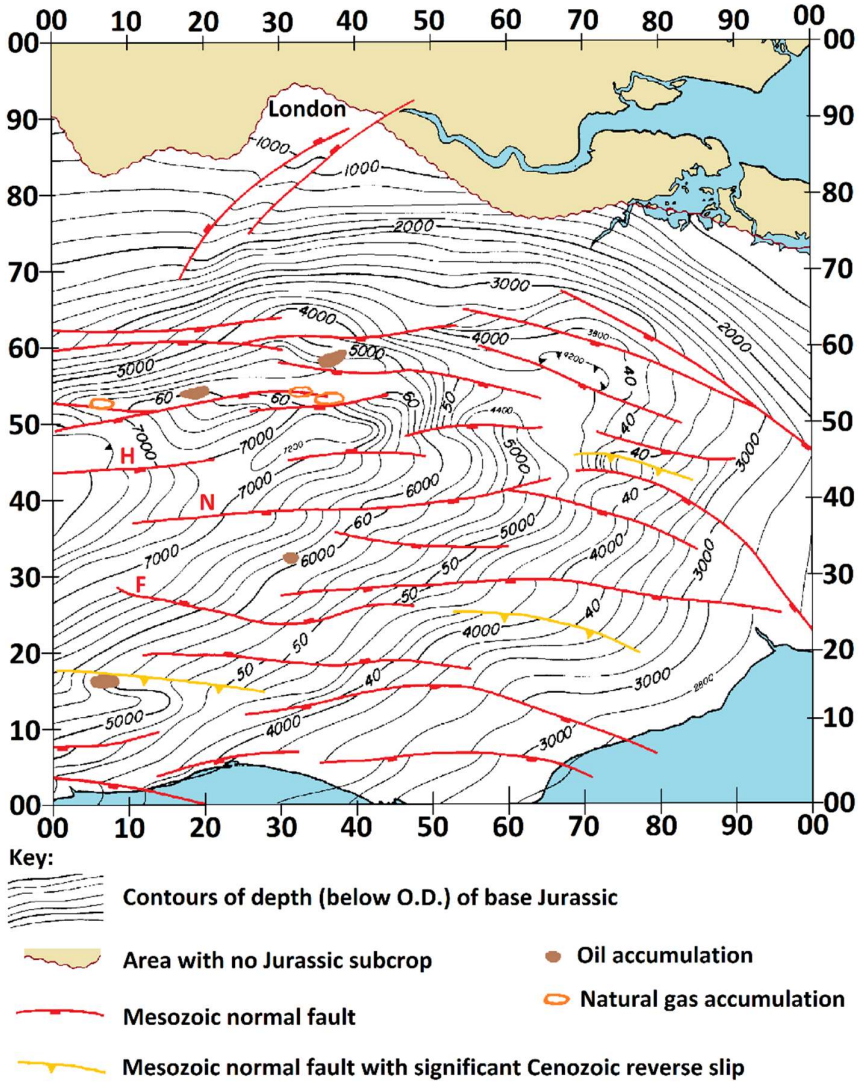
London
H
N
F
Key:
Contours of depth (below O.D.) of base Jurassic
Area with no Jurassic subcrop
Mesozoic normal fault
Mesozoic normal fault with significant Cenozoic reverse slip
Oil accumulation
Natural gas accumulation

Figure 6

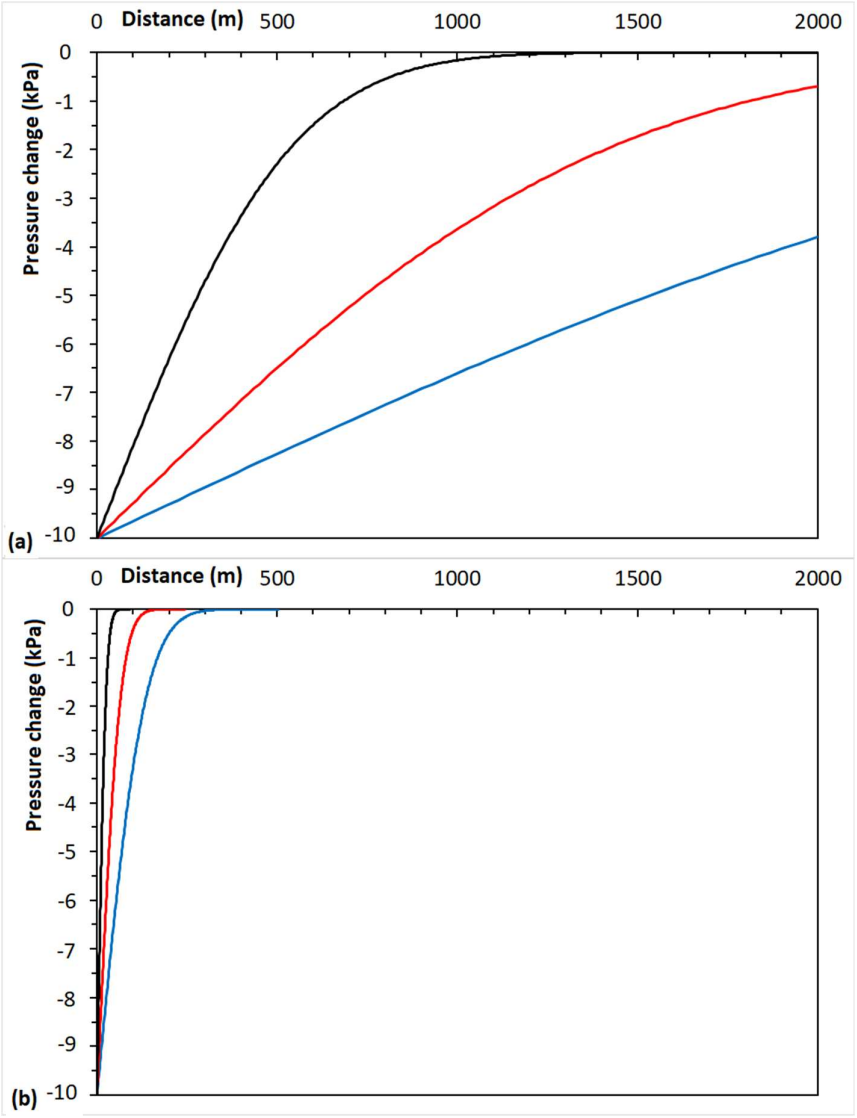
0
Distance (m)
500
1000
1500
2000
Pressure change (kPa)
0
-1
-2
-3
-4
-5
-6
-7
-8
-9
-10
(a)
0
Distance (m)
500
1000
1500
2000
Pressure change (kPa)
0
-1
-2
-3
-4
-5
-6
-7
-8
-9
-10
(b)

Figure 7

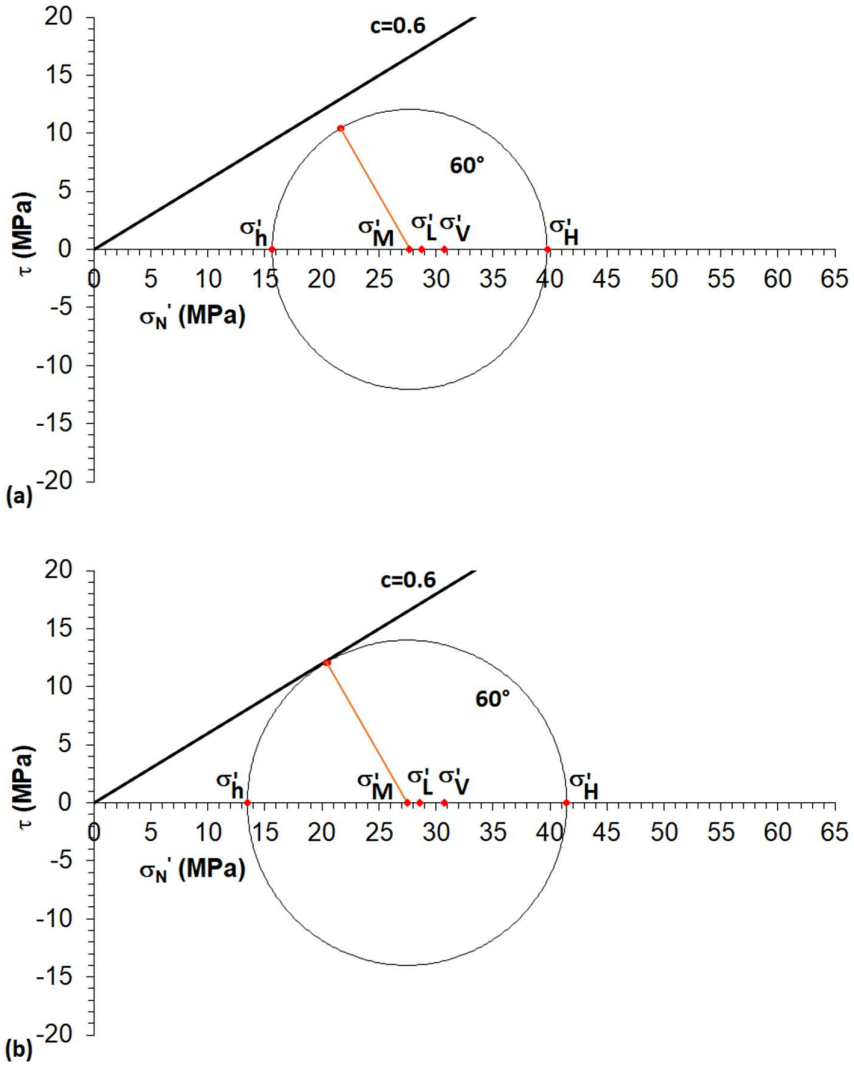

Figure 8